Faculdade de Engenharia da Universidade do Porto

U.PORTO

FEUP FACULDADE DE ENGENHARIA
UNIVERSIDADE DO PORTO

Development of a clinical app to predict the biomechanical behaviour of femur bones

Guilherme Faria Henriques

FINAL VERSION

Dissertation performed in the scope of the
Integrated Masters in Bioengineering
Major in Biomedical Engineering

Supervisor: Jorge Américo Oliveira Pinto Belinha
Co-supervisor: Renato Manuel Natal Jorge

June 2018

Abstract

Hip surgeries affect a large number of people with reports showing up to 7 million Americans being submitted to hip replacement surgery by 2015 and that number is expected to rise continuously. Despite this fact, in the present, there is no tool in a clinical environment which can provide relevant mechanical information to the physician in order to reduce the need for a revision surgery. Some relevant work has been done academically, regarding image segmentation, however those methods generally apply to secondary image modalities, such as MRI and CT scans. As defined by the AAOS, the clinical guidelines point towards using radiographs as the first imaging tool in hip injuries making this image modality of greater use in the clinical field.

In this dissertation, a background of information is given regarding the femoral bone and its anatomical, biological, pathological and mechanical perspectives. Following that, medical image modalities are explored and the theoretical principles behind them are explained. This is followed by a survey on the state of the art of image segmentation methods related to the topic of the present project. Moreover, a finite element method overview is given not only regarding its formulation but also its history with a heavier focus on the field of orthopaedics.

Lastly, the proposed clinical application is presented which, using femur x-ray radiographs, can process the femur computational model automatically and performs finite element analysis to assess the stress distribution in the bone. To perform this, the algorithm resorts to the radiograph's gradient to attain the computational model and with the evenly spread out mesh, executes a finite element analysis on the stress distribution calculating effective stress and its ratio to ultimate stress.

The obtained results allow the physician to assess the overall stress and damage level distribution if some considerations are taken when analysing the radiographs, such as the presence of artefacts and the presence of a meaningful contrast between trabecular and cortical bone.

Resumo

Cirurgias de anca afetam milhões de pessoas em todo o mundo, com estudos a demonstrarem que até 2015, cerca de 7 milhões de Americanos já sofreram uma artroplastia de anca ou de joelho. Este número é ainda espectável que continue a subir. Apesar disto, não existe atualmente uma ferramenta usada em ambiente clínico que providencie informação mecânica relevante para que uma cirurgia de revisão não seja necessária. Apesar de algum trabalho ter sido desenvolvido em âmbito académico em relação a segmentação de imagem, os métodos desenvolvidos geralmente aplicam-se à modalidade de imagens como ressonâncias magnéticas, ou TC's. A AAOS define, nas suas *guidelines* clínicas, que num paciente ortopédico a modalidade de imagem a ser usada deverá ser a radiografia e apenas em caso de dúvida se deve recorrer a outras modalidades. Este facto reitera a necessidade de existir mais tecnologia desenvolvida para a modalidade mencionada.

Nesta dissertação, é fornecida informação de contextualização em relação ao fémur e às suas perspetivas anatómica, biológica, patológica e mecânica. De seguida é explorado o tema de modalidade de imagens médicas, em que os princípios teóricos que as regem serão apresentados. Posteriormente, é apresentada uma pesquisa sobre o estado de arte de métodos de segmentação de imagem aplicados ao projeto em questão, procurando focar em radiografias. Após esta apresentação, é dada uma perspetiva global sobre o Método de Elementos Finitos não só sobre a sua formulação, mas também abordando a sua história com um foco especial na área da ortopedia.

Por último, é apresentada a aplicação clínica proposta na qual, usando radiografias de fémur, é possível realizar um processamento automático do modelo computacional e realizar análise de elementos finitos para avaliar a distribuição de tensões no osso. Para obter estes resultados o algoritmo recorre ao gradiente da radiografia para chegar ao modelo computacional, sendo capaz de gerar automaticamente uma malha uniforme e efetuar a análise de tensões, calculando a tensão efetiva e o seu rácio com a tensão máxima de compressão.

Os resultados obtidos permitem ao clínico avaliar a distribuição de tensões, tendo em conta algumas considerações com as radiografias, como a presença de artefactos e a presença de um contraste significativo entre osso trabecular e osso cortical.

Institutional Acknowledgements

Personal Acknowledgements

Ao longo do processo da dissertação e todo o caminho para aqui chegar, não caminhei sozinho. Felizmente, pude contar com amigos e família que me ajudaram nos tempos mais difíceis e com quem partilhei os momentos mais felizes.

À minha família, ao meu pai, minha mãe e minha irmã, quero agradecer a força e confiança que me deram sem me deixarem ir abaixo. Obrigado também pela ajuda, desde os aspetos técnicos até às situações mais casuais que me permitiram chegar onde cheguei.

Obrigado Isabel pelo teu amor, por acreditares em mim mesmo se eu não o fazia e por me ajudares a ultrapassar os meus objetivos, mesmo que nada tenham a ver com o curso. Também por ti sou a pessoa que sou hoje e a ti te devo isso.

Obrigado aos meus avós por sempre se preocuparem comigo e verem em mim uma pessoa em quem podem contar e orgulhar-se.

Obrigado às Alheiras pelos momentos de alegria, pelos jantares e pelos passeios. Espero que continuemos a reunirmo-nos para que esta tradição não se perca.

Obrigado aos meus amigos, pelo companheirismo seja nos momentos de encontro seja pela partilha de vídeos de Gato Fedorento.

Por último, gostaria de dedicar todo este meu percurso académico à minha avó que não estando presente para me ver terminar, tenho a certeza que ficaria cheia de orgulho por este momento.

A todos os mencionados e aos que, por lapso meu, não foram mencionados o meu muito obrigado.

Guilherme

Table of contents

List of figures

xiii

List of tables

Abbreviations

1D	One-dimensional
2D	Two-dimensional
3D	Three-dimensional
AAOS	American Academy of Orthopaedic Surgeons
CT	Computed tomography
DXA	Dual-energy x-ray absorptiometry
ECM	Extracellular Matrix
FE	Finite element
FEA	Finite element analysis
FEM	Finite element method
ICC	Intra-class Correlation Coefficient
IEEE	Institute of Electrical and Electronics Engineers
MRI	Magnetic resonance imaging
NHS	National Healthcare System
qCT	Quantitative computed tomography

Chapter 1

Introduction

1.1 - Motivation

A joint replacement surgery, particularly hip or knee replacement, is a highly complex procedure that affected 7 million Americans by 2015 [1]. This operation is steadily increasing with Canadian reports describing a 5-year increase 19.1% [2], and an expected increase of the number of hip replacement surgeries by 174% between 2005 and 2030 [3].

With patients living with a hip stem or a knee prosthesis, some complications may arise and affect the medical device. If the problem is threatening enough, it leads to a revision surgery in which the prosthesis is corrected or replaced if needed. These surgeries have seen an increase both in Canada [2] and the UK [4]. Adding to that, the economic impact of revision surgeries is immense, costing the NHS over £60 million in 2000 alone [4]. Moreover, it is clear that these surgeries are performed on younger people [1], which have greater physical demands, and, therefore, require solutions that can uphold those demands.

With the impact of these joint replacement surgeries, it is clear that something should be done to aid the decrease of these numbers. Thus, one possible solution is to help provide a subject-specific solution that diminishes the risk of a revision surgery occurrence.

To achieve this, one can make use of the several imaging techniques available to physicians. According to the Clinical Practice Guideline, by the AAOS [5], advanced imaging techniques, such as MRI or CT scans should only be considered if a hip injury is not apparent in initial radiographs. Therefore, radiographs are taken much more regularly than any other form of medical imaging for orthopaedics. This is backed up by the NHS data, which states that in a year, out of approximately 40 million medical imaging scans performed, 22 million singlehandedly belonged to x-ray radiographs, amounting to 55.2% of all scans [6].

1.2 - Goal of the project

With this project, the main goal is to help clinicians visualize and analyse patients' femur radiographs. Using a transversal software with automatic segmentation and finite element analysis, the ambition is to provide the clinician a computational model of his patient's femur

with stress and strain analyses available. As a result, the clinician should be able to more aptly decide on his patient's diagnosis and treatment from then on.

1.3 - Document's structure

This dissertation aims to introduce and describe the study performed in this year's second semester. As such, in the document's introductory chapter, the motivation and goal of the project are defined. Next, a contextualization of the different aspects involving the femoral bone, such as its anatomy, biology and mechanical properties, are explored. Following that, the theoretical basis of key medical image modalities is presented. Furthermore, a state of the art regarding medical image analysis and its segmentation methods is reported, focusing into femur radiograph. Moreover, a state of the art regarding the finite element method, along with the method's formulation, with its applications on orthopaedics, is described with detail.

After the contextualization component is finished this dissertation will focus on the project developed, giving a detailed explanation of its steps. Firstly, an introduction of the project is done followed by an overview of its steps employing a workflow to better understand the software's behaviour. Following this, the algorithm behind the software is thoroughly analysed and the software's interface is presented after that.

The document carries on with the presentation of the results and their discussion and, lastly, concludes presenting some future work to be developed in this field and the conclusions reached.

Chapter 2

Femoral Bone

2.1 - Introduction

In this project, the focus will be done on the analysis of the femoral bone. With this chapter, an analysis of this bone will be performed in its multiple attributes. Starting with its anatomical point of view of the femur, an examination will be performed describing its position and insertions and how it relates to its functions. Following that, a biological perspective, the focus will be on the constitution of bones both at a cellular and structural level. Lastly, the mechanical context of the femoral bone, such as the mechanical properties of the bone, is overviewed.

2.2 - Anatomy [7]

The human skeleton starts its composition with 270 bones which eventually fuse into 206 bones, in a healthy adult body. This body framework can be divided into two categories: axial skeleton and appendicular skeleton, in which the axial skeleton consists of the spine, the rib cage and skull (accounting also for its associated bones) and the appendicular skeleton is constituted by the shoulder and pelvic girdle and the bone part of the upper and lower limbs. This set of organs has as its main functions the support and protection of the human body.

The femoral bone is part of the appendicular skeleton. It is located inferior to the pelvis and it is articulated to two structures. Proximally, the femur articulates with the acetabulum forming the hip joint, while distally, the femur articulates with the patella and tibia forming the knee joint.
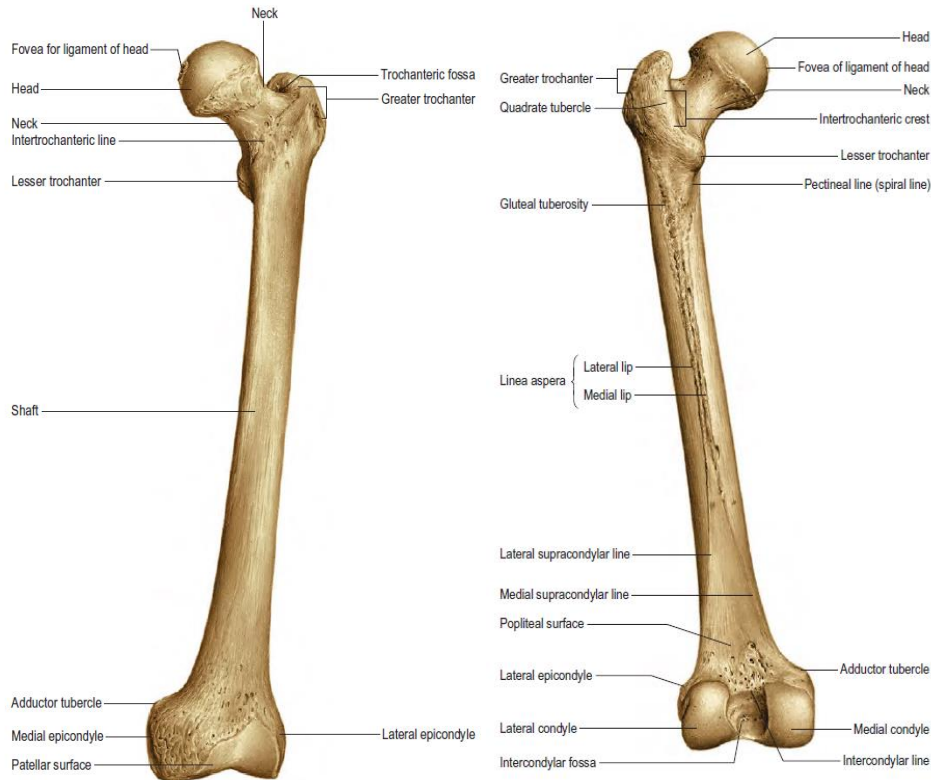
Figure 2.1 [7] – Representation of the femoral bone (anterior aspect)

As visible in figure 2.1, the femur is a long bone, being the longest bone in the human skeleton, having its size varied according to the patient's height. The bone itself presents several structures, which help the femur fulfil its supportive functions.

The semi-spherical head performs the connection with the pelvis' acetabulum and it contains a small rough area in its surface called the fovea, in which the *ligamentum teres* links the femur to the pelvis. Still in the proximal portion of the femur, two trochanters are present: the greater trochanter and the lesser trochanter. The greater trochanter is a large and quadrangular structure that projects itself in a superomedial direction. In its highest point, the greater trochanter reaches the midpoint of the hip joint. The lesser trochanter is a conical posteromedial projection which serves as an insertion for the iliacus muscle and the psoas major muscle. The shaft consists of the long cylindrical-shaped body of the femur. This structure is narrowest in its centre, having a small expansion proximally and a larger one distally and in its posterior surface contains a *linea aspera* that works as a muscular insertion for several hip and thigh muscles.
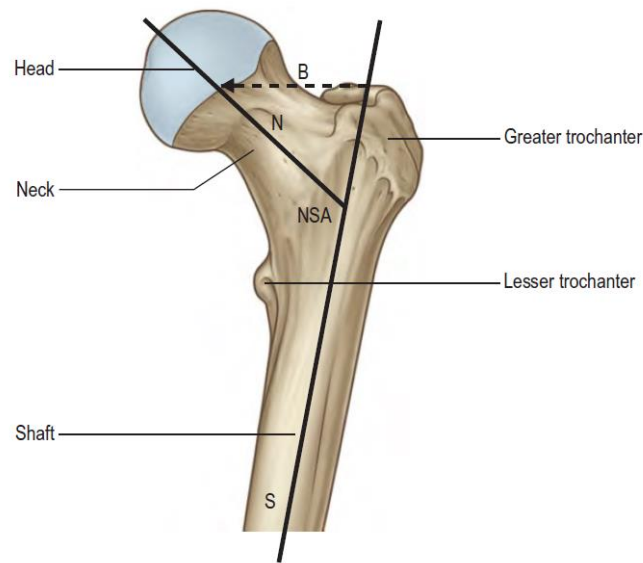
Figure 2.2 [7] – Representation of the neck-shaft angle (NSA). The angle between the long axis of the femoral shaft (S) and the axis of the femoral neck (N) is on average 135˚ (range 125–140˚)

Between the shaft and the femoral head, the neck connects these two structures at an average angle of 135º. It is a 5 cm long, approximately, complex that enables the limb to swing clear from the pelvis. Distally, the femur creates the knee joint making use of the lateral and medial condyle, the intercondylar fossa and the patellar surface. The condyles are two smooth structures that, when combined with the patellar surface make an inverted U shaped articular surface that will contact with the tibia and patella. Both the medial and lateral condyles have a medial and lateral epicondyle projecting out of them, respectively. The walls of the intercondylar fossa function as the insertion of both the anterior cruciate ligament (ACL) and the posterior cruciate ligament (PCL), which has heavy importance in the stabilization of the knee joint.

2.3 - Biology

Bones have an intricate composition at the microscopic level. The mature cellular components of the bones are divided into 3 components: osteoblasts, osteoclasts and osteocytes [7].

Osteoblasts are bone forming cells, meaning they are responsible for the synthesis, deposition and mineralization of bone matrix. These cells secrete type I collagen and small amounts of type V collagen that will be part of the extracellular bone matrix (ECM). Osteoclasts are large polymorphic cells which central purpose is the removal of bone during bone growth. They cause the demineralization of the ECM by releasing lysosomal and non-lysosomal enzymes. Lastly, osteocytes constitute the major type of mature bone cell and they are scattered throughout the bone matrix. These cells are relatively inactive, however they do play an important role in the maintenance of bone as their death leads to resorption of the matrix by osteoclast activity. It can also occur that osteocytes are mineralized and will then be part of the bone's ECM. It is also worth noting that once osteoblasts are integrated into the bone matrix they turn into osteocytes [7].

Bone remodelling is an important activity performed by the different bone cells. The overall process aims to renew bone tissue through the regeneration of both the ECM and osteocytes. In order to perform this task, a synchronized activity of osteocytes - removing old bone tissue – and osteoblasts – creating new ECM – allows for the maintenance of a healthy bone [7].

Despite being mentioned, the ECM is not yet examined in this work and said examination will be executed in this paragraph. The bone's extracellular matrix is comprised of an organic component – 35% - and an inorganic component – 65% [8]. The organic components consist of mainly type I collagen fibres, which makes up of around 90-95% of the organic portion, while the remaining organic component comprise of proteoglycans rich in hyaluronic acid. The collagen fibres have a highly ordered arrangement with changing orientations and they provide elasticity and tensile strength [9]. As for the inorganic components, it mainly consists of calcium deposits with the characteristics of hydroxyapatite [8]. These deposits grant stiffness to the bone along with a great compressive strength [9]. The mineral component alone, despite its great stiffness is a very brittle material, however when combined with the type I collagen it creates a material with great tenacity.

Despite the constituents of bone being the same throughout a single bone, their distribution varies greatly. The distribution follows two different patterns that are divisible into two groups: cancellous or trabecular bone, and cortical or compact bone.

Calcar femorale
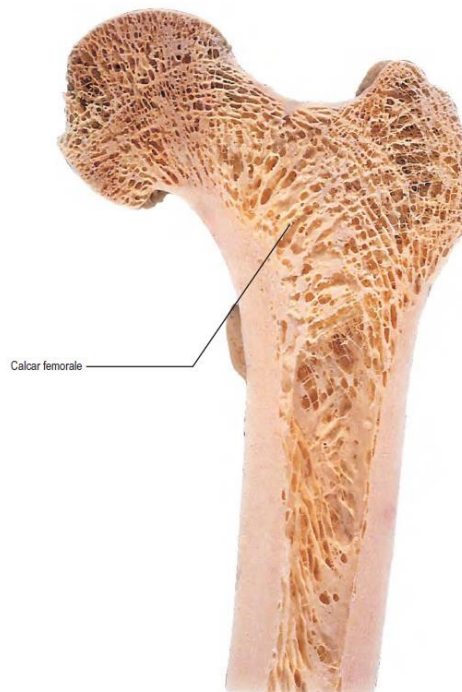
Figure 2.3 [7] – Coronal section of the femur displaying the difference between trabecular and cortical bone

Cortical bone is a dense organization of the bone matrix and presents itself on the exterior portion of bone. This type of macroscopic distribution accounts for around 80% of the human body and provides the bone's strength. Trabecular bone, however, is usually located in the interior of bones and, while it provides some strength to the overall structure, its main function is supporting bone marrow and allowing for the bone to have a combination of good strength while maintaining a low weight, reducing the density of the bone [7].

2.4 - Pathologies [10]

Bone diseases have great impact in a patient's life condition. By decreasing the bone's condition, it presents a dangerous menace of bone fracture. These disorders, while differing in impact size, can occur at any age group. In this subchapter, osteoporosis will be tackled, a pathology that most affects patients at an advanced age, especially menopausal women (figure 2.4), and osteosarcomas, which most frequently affect children and adolescents until the second decade of life, around 60% of total patients with this condition.
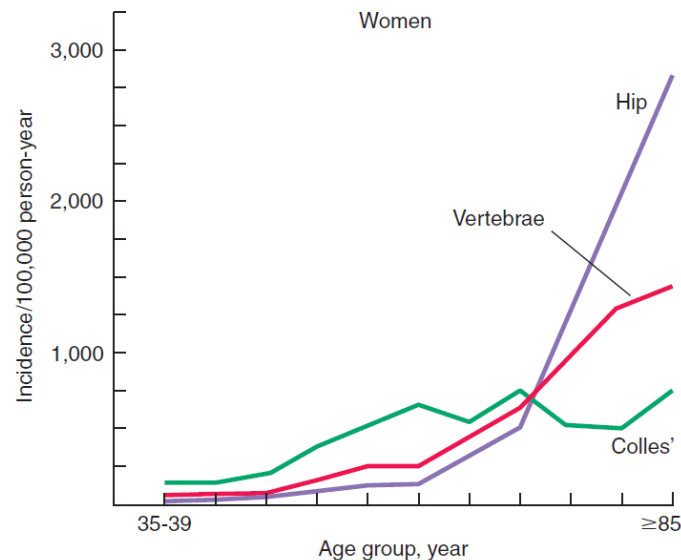
Figure 2.4 [10] – Epidemiology of vertebral, hip, and Colles' fractures with age for women

Osteoporosis is a greatly impactful bone disease that is very common for older aged patients. This disease is defined as a reduction in the strength of bone that leads to an increased risk of fractures through deterioration in skeletal microarchitecture. In the United States, as many as 8 million women and 2 million men have osteoporosis and an additional 18 million individuals have bone mass levels that put them at increased risk of developing osteoporosis.
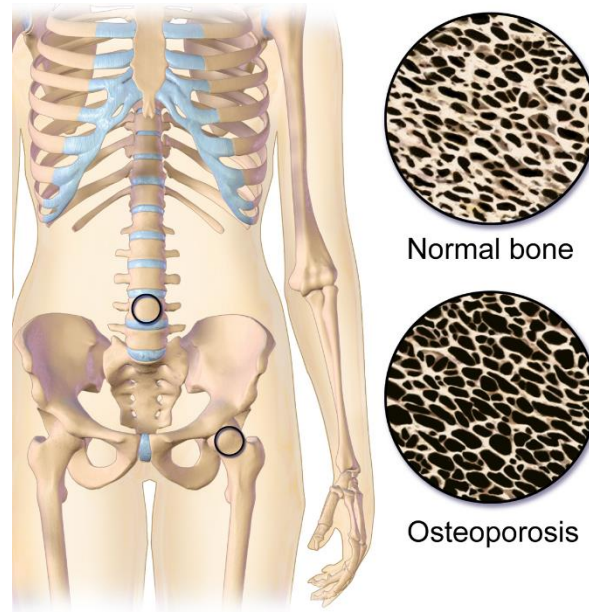
Figure 2.5 [11] – Representation of the architectural structure of normal bone compared with an osteoporotic bone and the most common occurrences of osteoporosis

As previously stated, this disease leads to a higher risk of fracture and, depending on the health and age of the patient, this health condition can become a severe limitation for the patient's abilities in moving and performing simple activities.

The appearance of tumours in bone tissue can also pose a serious threat to bone health and its ability to execute its functions. When the tumour is cancerous, it is called osteosarcoma. The malignant cells will form a tumorous mass that will commonly appear in the extremities of long bones and will corrode its matrix, which severely decreases its mechanical properties and increases the fracture risk.

2.5 - Mechanical properties [12]

As stated in previous chapters, bone can be classified into two categories according to its macroscopic architecture as cortical or trabecular bone with contrasting apparent densities. The mechanical properties of bone depend therefore of the composition of each bone type and its porosity.

Apparent density, ρ_{app}, can be defined as the division of the wet mineralised mass of bone sample, w_{sample}, over the volume occupied by the same sample, V_{sample}, as seen in equation (2.1).

$$\rho_{app} = \frac{w_{sample}}{V_{sample}} \tag{2.1}$$

The apparent density of cortical compact bone is of around 2.1 g/cm^3. Knowing the porosity, p, see equation (2.2), of a certain bone, it is possible to obtain the apparent density of said bone by correlating to its porosity, as shown in equation (2.3), in which ρ_0 corresponds to the compact bone apparent density.

$$p = \frac{V_{holes}}{V_{sample}} \tag{2.2}$$

$$\rho_{app} = \rho_0 \cdot (1 - p) \tag{2.3}$$

In 1991, Lotz [13] proposed a phenomenological material law to estimate the elasticity modulus for both trabecular and cortical bone along with ultimate compressive stress. This was a pioneering work, allowing to determine the mechanical properties using different laws for cortical and trabecular bone and considering the anisotropic nature of bone. The equations for determining the Young's modulus and the ultimate compressive stress are expressed in equations (2.4) and (2.5), respectively, with the coefficients presented in table 2.1.

Bone Tissue	Direction	a_1	a_2	a_3	a_4
Cortical	Axial	2.065E+03	3.090E+00	7.240E+01	1.880E+00
	Transversal	2.314E+03	1.570E+00	3.700E+01	1.510E+00
Trabecular	Axial	1.904E+03	1.640E+00	4.080E+01	1.890E+00
	Transversal	1.157E+03	1.780E+00	2.140E+01	1.370E+00

Table 2.1 [12] – Coefficients of Lotz's Law

$$E_i = a_1 \cdot (\rho_{app})^{a_2} \tag{2.4}$$

$$\sigma_i^c = a_3 \cdot (\rho_{app})^{a_4} \tag{2.5}$$

More recently, in 2008, Zioupos [14] has published an experimental study in which the results show that the relation between E_i and ρ_{app} is not an increasing monotonic function as demonstrated with Lotz's law, but instead has a boomerang-like pattern. Later, using the data from Zioupos, Belinha [12] proposed that the law determining the mechanical behaviour of bone tissue is the same for both cortical and trabecular bone. Thus, following the results and conclusions obtained in Zioupos' work, Belinha [12] proposed a new mathematical model for determining the Young's modulus and ultimate compression stress, found in equations (2.6) and (2.7), for axial directions with the coefficients found in table 2.2.

Coefficient	$j = 0$	$j = 1$	$j = 2$	$j = 3$
a_j	0.000E+00	7.216E+02	8.059E+00	0.000E+00
b_j	-1.770E+05	3.861E+05	-2.798E+05	6.836E+04
c_j	0.000E+00	0.000E+00	2.004E+03	-1.442E+02
d_j	0.000E+00	0.000E+00	2.680E+01	2.035E+01
e_j	0.000E+00	0.000E+00	2.501E+01	1.247E+00

Table 2.2 [12] – Coefficients of the proposed bone tissue phenomenological model

$$E_{axial} = \begin{cases} \sum_{j=0}^{3} a_j \cdot (\rho_{app})^j \ \ if \ \rho_{app} \leq 1.3 \ g/cm^3 \\ \sum_{j=0}^{3} b_j \cdot (\rho_{app})^j \ \ if \ \rho_{app} > 1.3 \ g/cm^3 \end{cases} \tag{2.6}$$

$$\sigma_{axial}^c = \sum_{j=0}^{3} d_j \cdot (\rho_{app})^j \tag{2.7}$$

In figures 2.6 and 2.7, the relation between elasticity modulus and apparent density and the relation between ultimate compression stress and apparent density are displayed, respectively, both in the axial direction. In addition, it compares the model proposed in Belinha's [12] work with the Lotz's [13] model.
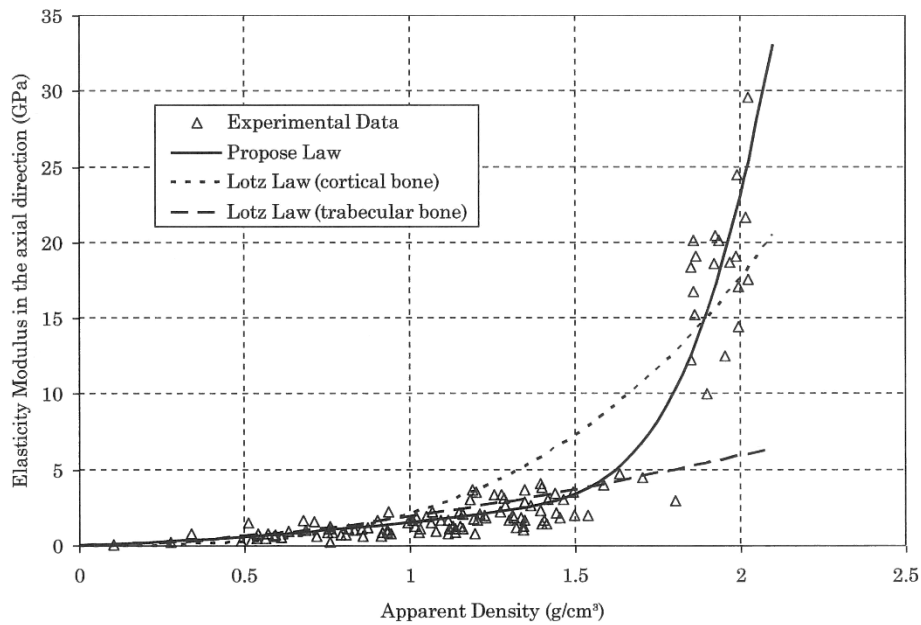
Figure 2.6 [12] – Relation between elasticity modulus in the axial direction and apparent density following the proposed law and Lotz's law with Zioupos' [14] experimental data
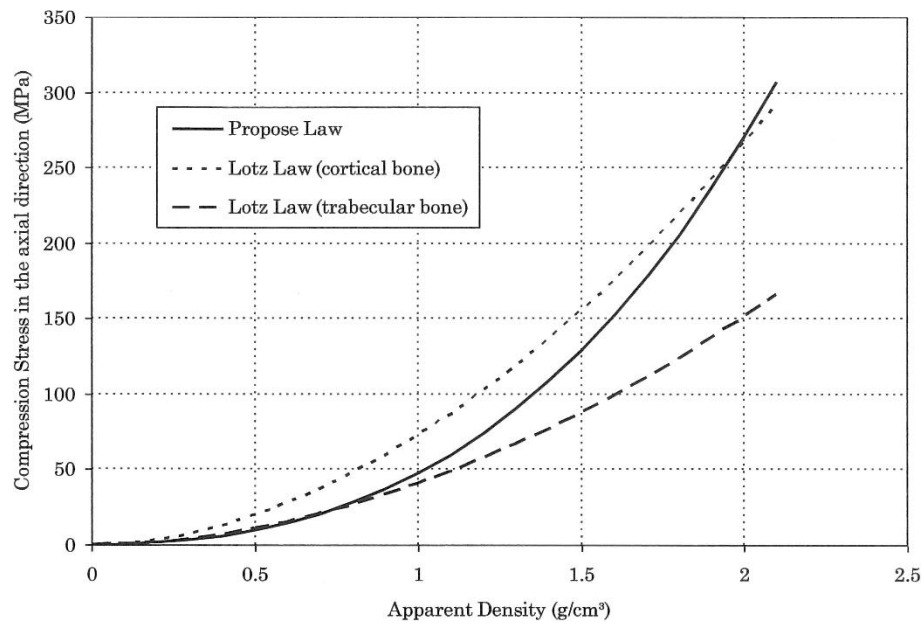
Figure 2.7 [12] – Relation between compression stress in the axial direction and apparent density following the proposed law and Lotz's law

As figure 2.6 shows, the law proposed by Belinha correlates better with the experimental data than the two proposed Lotz's curves (for trabecular and cortical bone).

12

Chapter 3

Medical Imaging

3.1 - Introduction and History

Medical imaging refers to several different techniques that are used to observe the human body in order to diagnose, monitor or treat medical conditions [15]. These techniques have shown an incredible utility in its use for the aforementioned objectives with over 5 billion investigations worldwide up until 2004 and with visible growth in its use [16].

The discovery of medical imaging modalities began in 1895 with Wilhelm Röntgen seeing the bones in his hand on a photographic plate on the other side of an electron beam tube [17]. With this fortunate accident, radiography was born and made way for several other image modalities to be researched in its future.

In March of 1973, Paul Lauterbur [18] published a theoretical paper on how one object could be visualized by taking advantage of its local interactions. By applying a static magnetic field, the interactions within a sample object can provide us with an image of itself and, with this paper the theoretical basis for magnetic resonance imaging was found. This work was later on validated with Herman Carr providing a 1D nuclear magnetic resonance spectrum in its PhD thesis [19].

Concerning computed tomographies, its mathematical foundation was found in 1917 with the Radon transform [20]. With this integral transform, one is able to find the original density of a certain object from its project data in a tomographic scan. Despite its early theoretical support, solely in 1963 was the first primitive CT scan machine developed with its patent attributed to William H. Oldendorf [21].

Though several other techniques exist, such as ultrasound or even infrared spectroscopy, the three mentioned techniques will be focused on, explaining its mechanism and use in medical situations.

3.2 - Magnetic Resonance Imaging – MRI [22]

Magnetic Resonance Imaging is an imaging method based principally upon sensitivity to the presence and properties of water, which makes up 70% to 90% of most tissues. In each tissue, the amount of water and its properties can alter dramatically with disease and injury.
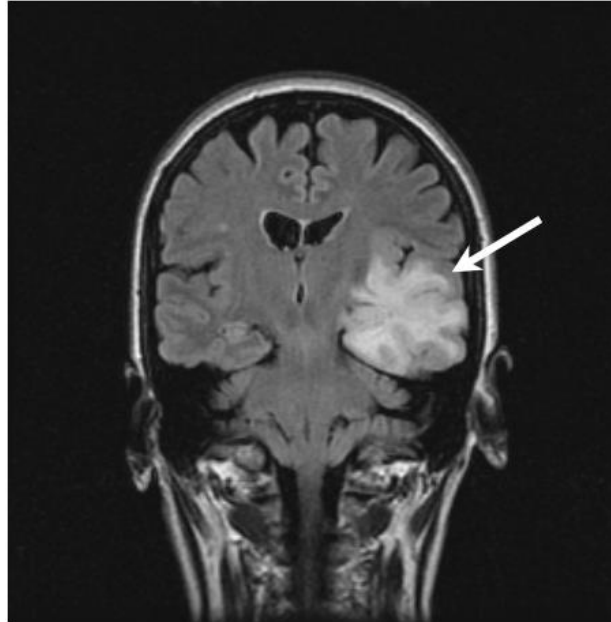
Figure 3.1 [22] – Coronal scan of a brain indicating a tumour (arrow)

The mechanism of this image modality relies on the polarity of the water molecule and its interaction with magnetic fields. Energy from an oscillating magnetic field is applied to the patient at an appropriate resonance frequency. The energy is absorbed by the protons of the water molecules (H^+) affecting their natural spin. After the magnetic field pulse is switched off, the protons begin to relax and obtain their natural spin. The dephasing between relaxation times generates the contrast visible in the MRI scans.

The properties that most affect the scan contrast are proton density – PD – and two characteristic times called spin-lattice relaxation time and spin-spin relaxation time, denoted T1 and T2 respectively. Proton density refers to the number of hydrogen atoms a certain tissue has; while fluids such as blood have higher PD (due to its higher water percentage) other tissues, such as tendons or bones, have smaller PD due to its lower water presence.

This imaging technique is a highly sophisticated one and requires expensive and complex machinery to run. This explains the fact that it was the 4th most used imaging technique between January of 2016 and January of 2017, in the UK, with approximately 3.2 million scans performed [23]. Nonetheless, it has great utility and is a highly relevant medical imaging modality.

3.3 - Computed Tomography – CT [24]-[25]

Computed Tomography comes in many different forms. From single-photon emission computed tomography – SPECT – to simple X-ray CT. In this chapter the focus will be on X-ray CT since it is the most commonly used form of this image modality, especially in the orthopaedic field.

This image modality is operated by using an X-ray generator that is rotated around a patient, with an X-ray detector on the opposite side retrieving several scans (the mechanism behind the X-ray scan will be explained in the coming subchapter). Since the machine knows the positioning for each scan taken, it can use the 2D scans to create a series cross-sectional images. Once the slice thickness is taken into account, a 3D representation of the series is easily achievable.

In each 2D scan, the image modality is measuring the X-ray attenuation of the tissue. Therefore in each pixel, the darker it gets, the lower the attenuation is. This is measured with Hounsfield units that ranges from +3071 (most attenuating) to -1024 (least attenuating). This image modality can also rely on injected contrasts to provide a clearer image of a tissue. As long as the contrast has a meaningful difference in attenuation, it should provide a clearer image to the physician.
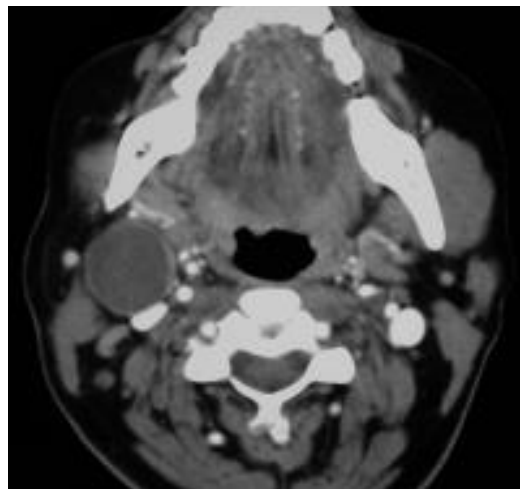
Figure 3.2 [25] – Cross-sectional CT scan of the neck of a patient

CT scans are currently widely used, with reports showing numbers up to 13.2 million scans in France (in 2015) and 11.6 million scans in Germany (in 2014) performed [26]. Being a state of the art technology that provides 3D information on a patient, makes it a very attractive solution. However, due to its cost in use, it is not recommended as a first line diagnostic tool, as seen in the first chapter [5].

3.4 - X-ray Radiographs [27]

As mentioned in the introductory chapter, this image modality has frequent use, being the main image modality used in the orthopaedic field.

For this image modality, a series of excited photons are projected onto the patient's body by an X-ray generator. These photons can then either be interact with tissue or pass through it. In either instance, its result is captured by an X-ray detector placed on the other side of the body portion aimed to be evaluated.

A photon can interact with matter in several forms. The predominant three interactions are the photoelectric absorption, Compton scattering and Rayleigh scattering. In the first interaction, the photon's energy is absorbed by an electron leading to its ejection with or without kinetic energy depending on the energy absorbed. Compton scattering occurs if the photon's energy is well above the ionization energy required for an electron to be removed from an atom. In this case, only part of that energy is transferred to an electron while the photon remains with energy following a different direction. Lastly, regarding Rayleigh scattering, despite having a low energy interaction, this interaction is still significant when it comes to lower energy scans, such as mammograms. In it, a photon is absorbed by an atom and is immediately released with the same energy but with different direction.

These interactions cause the photons to lose their energy which is in store absorbed by the tissue, creating the contrast in the image. However, being an ionizing radiation it is quite harmful for living tissue, with radiation overexposure being linked to the appearance of cancerous tumours, with the World Health Organization classifying X-rays as carcinogen [16].

Since bone has a high amount of calcium, which is a high atomic number atom, bones easily absorb X-ray waves, which makes them stand out from remaining tissues in this image modality, also making it perfect to use in an orthopaedic environment. The result of a projectional radiograph can be seen in figure 3.3, in which the bone clearly stands out from the remaining tissue.

Figure 3.3 – Hip X-ray radiograph displaying bone in a much brighter colour than its surrounding tissue

Chapter 4

Image Segmentation

4.1 - Introduction

Image segmentation is one of the primary steps in to build a patient-specific finite element model of a bone. After performing image acquisition, the segmentation step allows for the creation of an accurate geometric model of the bone domain, femur in this particular instance. In this chapter, an overview of segmentation techniques applied to different fields and image modalities previously delineated will be presented, increasingly funnelling to the situation at hand. A special focus will be given to techniques that apply to femur using radiographs.

4.2 - General overview

With the evolution of computer-aided diagnosis — CAD — and overall technologic influence in medicine, image segmentation has shown to be a crucial stage and has gained great advances in its medical application, especially in the last 30 years with the improvement of the several image modalities.

Several articles mark significant advances in medical image segmentation. Vincent et al. [28] first introduced, in 1991, the watershed method for image segmentation, practice which is now commonly used in image segmentation of different modalities. Another example is given to us by Yezzi et al. [29] who implemented active shape models, commonly known as snakes, to medical images and that method attracted the attention of the research community, having at least 262 paper citations, according to IEEE.

Despite the examples presented having applicability across multiple modalities, in some situations it is better to accommodate the segmentation method to the image modality in question. Noble and Boukerroui [30] presented an influent review paper on image segmentation methods on ultrasound. Despite presenting some methods that either could be generalised to different modalities, such as Chalana and Kim's [31] and Mitchell et al.'s [32] techniques, most methods are specific to ultrasound and its applications. Considering cardiac ultrasound, Friedland and Adam [33] presented a pioneering work allowing the detection of cavity boundaries using simulated annealing, which is an optimisation algorithm with a Markovian spatio-temporal regularisation. At the same time, Mulet-Parada and Noble [34] proposed a local-phase-based approach to spatio-temporal endocardial border detection, arguing that local phase is a better basis for ultrasound-based feature detection and segmentation because local

phase is theoretically invariant to intensity magnitude. Alternatively, if breast cancer is considered, the work developed by Stavros et al. [35] greatly influenced the design of algorithms for breast mass detection as is seen in later publications, such as Drukker et al. [36], where mass detection is performed by first filtering the images with a radial gradient index filtering technique and, with it, thresholding occurs to delineate lesions.

When the focus is shifted to femur, several segmentation techniques can be found with high-end imaging techniques. Yan Kang et al. [37] suggested an adaptive region-growing method for femur segmentation on CT scans. Following the first region-growing step, some adjustments were performed in order to obtain a closed and smooth boundary. Along with this work, several others were based on CT scans to obtain a femur model, such as Saha and Wehril [38], who used a fuzzy distance transform based thickness to segment a femur, and Kaus et al. [39], who used a priori knowledge to build a 3D point distribution model of a femur.

For this work 2D radiographs will be used, therefore looking for segmentation methods that are adapted to that reality is vital.

4.3 - 2D x-ray segmentation techniques

As previously mentioned, X-ray is a frequently used image modality, but of which few segmentation methods exist in literature. To gather information on diverse methodologies required an extensive search activity, whose epitome will now be presented.

Baka et al. [40] presented a reconstruction of the distal femur using a statistical-shape model. In it, they use CT scans as training data to build an average point distribution 3D femur model. For each radiograph, the 3D model is projected in two dimensions, and using Canny edge detection, the model's landmarks are adapted to the nearest edge. For each projected landmark, the 3D distance and angle is calculated between the 2D edge point and the original 3D landmark point. These two values become part of the energy value, and it is precisely this value which the method aims to minimize. To calculate it, the authors use the equation represented in (4.1), in which $u_i(p_j)$ serves as a mask for points that fall on projection i or not, $w_i(p_j)$ determines the orientation weighing term, which is equal to $\cos(\alpha)$ for every calculated angle below 90º, and, lastly, $D_i(p_j)$ establishes the distance term. Its calculation is visible in equation (4.2), where v controls the smoothness of the exponential. An overview of this method is seen on figure 4.1.

$$\Theta_i(p_j) = 1 - u_i(p_j) * w_i(p_j) * D_i(p_j) \tag{4.1}$$

$$D_i(p_j) = \exp\left(-\frac{d_i(p_j)}{v}\right) \tag{4.2}$$
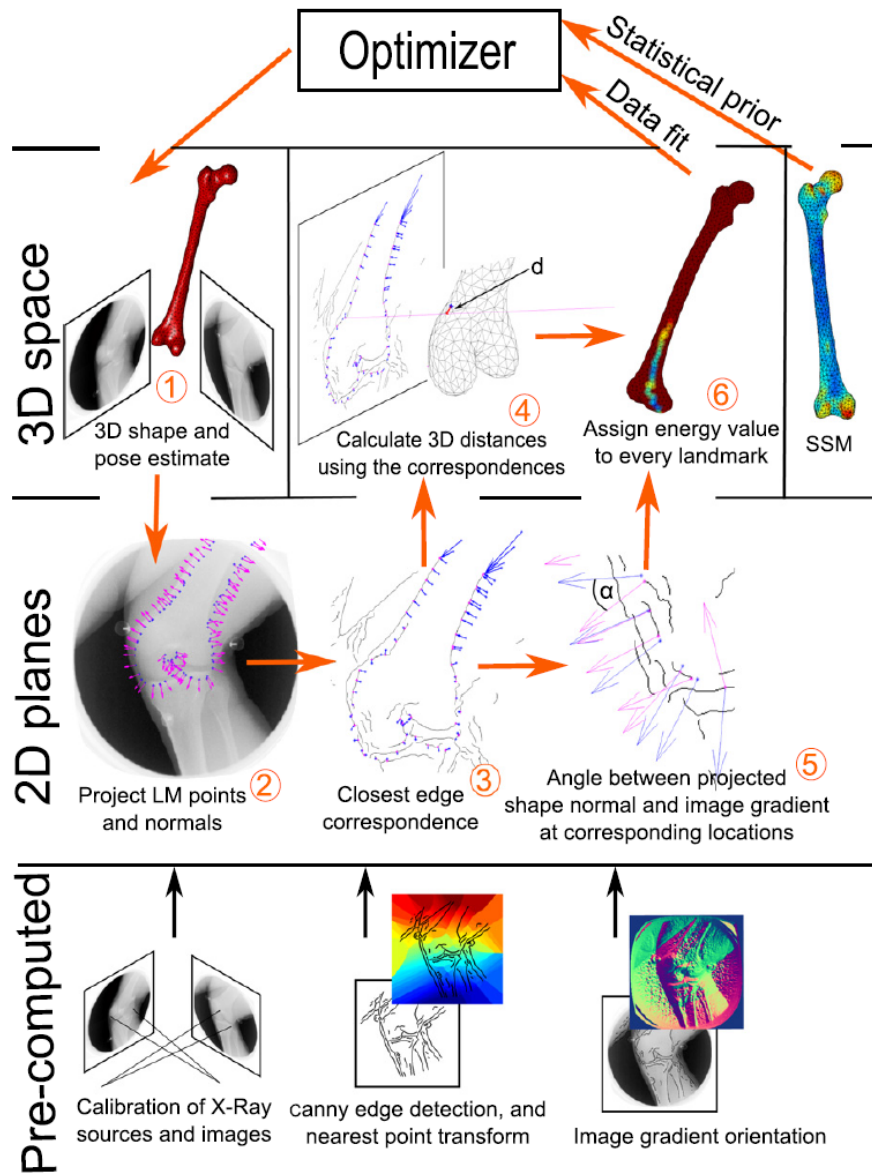
Figure 4.1 [40] - Overview of the steps taken to generate the model and calculate its energy value

Since a database of CT scans is not available, it is not possible to replicate this method. However, some techniques such as the Canny edge detection show great usefulness in the attainment of a 2D femoral model.

Bandyopadhyay et al. [41], more recently, presented an approach for long-bone fracture detection, tested on femoral bones, in which the segmentation is a pivotal initial step. In this study, the authors, after studying different segmentation methods opted to select an entropy-based algorithm. With it, local entropy is calculated in a 9x9 window, and in the biggest transitions the largest entropy should be identified due to varied local intensities. The outcome can be seen in figure 4.2. From this pre-processed image, the contour generation is done by using adaptive thresholding in an 8-neighbouring window. If a pixel has a value higher than the

adaptive threshold suggested, it will be part of the contour. This final contour is exemplified in figure 4.2.
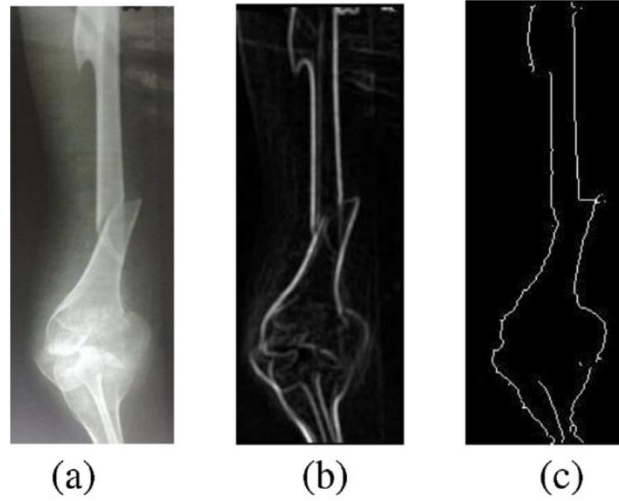
Figure 4.2 [41] - (a) Original digital x-ray of broken femur, (b) pre-processing using local entropy computation and (c) contour generation based on the image obtained in (b)

To correct the contour obtained, the authors introduce a method they named relaxed digital straight line segments — RDSS. In this approach, Bandyopadhyay et al. [41] use chain code to characterize a close-ended digital curve and define 2 properties it must follow:

- R1 - The runs have at most two directions, differing by 45°.
- R2 - Both directions can have at-most three run lengths, which are consecutive integers.

By applying these properties to the contour, they create a simplified version of the generated contour. After using this technique, the algorithm is able to amend any discontinuities present due to the parallel property in consecutive line segment. The final result is seen in figure 4.3.
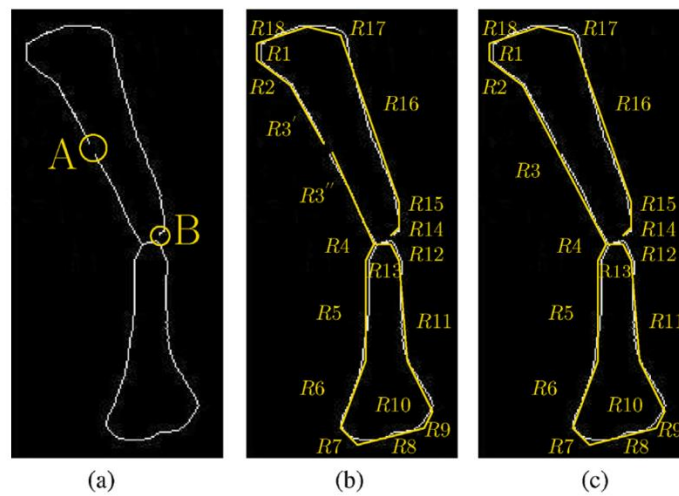
Figure 4.3 [41] - (a) Generated contour with discontinuities at A and B, (b) contour with RDSS applied and (c) contour with RDSS and no discontinuities

This work has a closer proximity to the conditions of the work to be developed and therefore, a lot more information can be recovered and used in the future.

One last work with high relevance is the one developed by Chen et al. [42]. In this work, Chen et al. present a method for segmenting the femur from hip x-rays with access to a set of training data. To do this, the authors try to identify three features: the femoral shaft, the femoral head and the turning point at the great trochanter. For each feature, they retrieve several candidates, which later on will be selected by the best fit. For the femoral shaft, the horizontal gradient is measured and scanned horizontally. The regions with a local maximum horizontal gradient will be selected as possible borders of the femoral shaft. The contour following method allows for the generation of each line. After obtaining several line candidates, the lines are paired by having the width closest to the training sample. For each pair of lines a probability value is attributed following the equation in (4.3), in which P_i is the probability value, M_i is the mean intensity gradient magnitude along the line and $G(w_i|\mu, \sigma)$ is the Gaussian of the width w_i in a distribution with μ average and σ standard deviation.

$$P_i = M_i \cdot G(w_i|\mu, \sigma) \tag{4.3}$$

The pair of lines with the highest probability value is selected. For the femoral head, the vertical and horizontal gradients are computed, since the femoral head has a round shape both gradients should have a high value. From the top left region, a circular Hough transform is fitted over the points with higher gradient to obtain circles shaping the femoral head. To fit the best candidate, a different probability value is calculated through equation (4.4), in which it equals to the Gaussian of the ratio between each candidate radius and the width of the previously selected shaft.

$$P_i = G(r_i/w|\mu, \sigma) \tag{4.4}$$

In order to detect the turning point at the great trochanter, the femoral shaft outside border is extended upward continuing the border using the contour following method. After this, the second derivative is computed and the point with the highest second derivative is defined. In figure 4.4, a representation of this method applied to a single radiograph is presented.
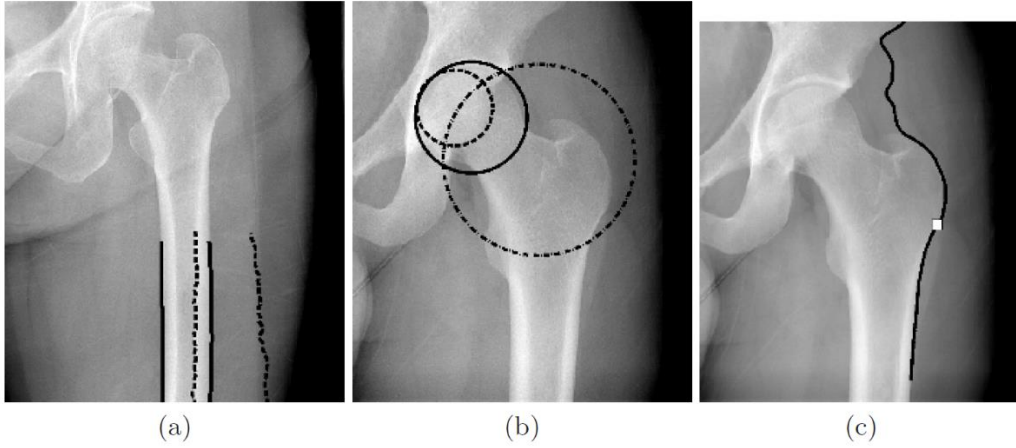
Figure 4.4 [42] – (a) Candidate femoral shafts, (b) candidate femoral heads and (c) turning point (white point) at the great trochanter

After these features are extracted, an average model generated from the training samples is superimposed in the image. With it, a piecewise registration is performed. Using the features obtained above, the average model selects five feature points: the most top and the most left point in the femoral head border, the turning point, and the bottom two points in the femoral shaft. The piecewise registration is calculated according to equation (4.5), in which q represents the image feature point, p represents the model's feature point, s represents a scaling factor, R represents a rotation matrix and, lastly, T represents a translation vector.

$$q = s\,R\,p + T \tag{4.5}$$

As the last step, in order to adapt the model to each individual femur, an active contour, commonly known as snakes, is applied. This better adjusts the model to the image at hand, as it is visible in figure 4.5.
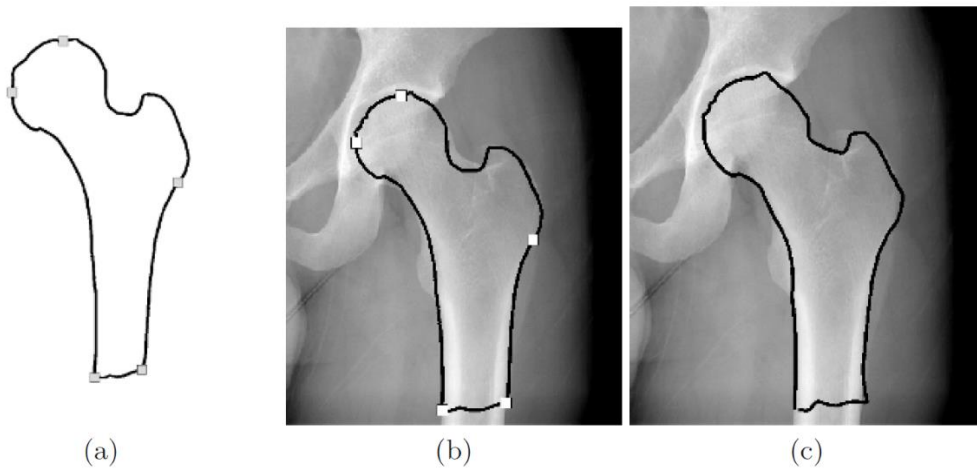
Figure 4.5 [42] – (a) Model femur contour divided into five segments, (b) piecewise registered femur model used as the initial configuration of the snake algorithm and (c) Extracted femur contour after running the snake algorithm

This work proposed in 2005 [41] has great relevance for the work to be developed here since both have similar conditions. The geometric approach to the femur segmentation seems adequate, since this particular bone has several unique geometric features, which, as it is perceptible in Chen et al.'s work, can be exploited to benefit this work.

From the work developed by Chen et al. [41], a lot was used. The use of the vertical and horizontal gradients was applied further on to the detection of femoral borders which allowed for the creation of a computational model.

24

Chapter 5

Finite Element Method

5.1 - Origins

Finite element analysis has its origins in 1940's. With the emergence of digital computation, a conceptual approach to finite element analysis arose with Courant's article [43]. However to put it in practice was a long and shared effort, that culminated in the paper written by Turner, Clough, Martin, and Topp [44], henceforth known as TCMT, in which the term finite element analysis was first coined. This method has great utility since it allows for modelling and discretization of several physical phenomena and history showed its eclectic application range. FEA was firstly used in physics in 1957 [45], however its big leap was when Argyris published a book on the use of FEM in aerospace engineering [46]. This development of finite element analysis was a consequence of a combination of several ingredients, one of which was digital computing. This technology was only affordable to this industry through mainframe computers [47].

From this start, the application of FEM began to branch out to several different fields. The piecewise analysis allowed it to be applied to fluid mechanics, electromagnetic fields and thermal and mass transport analysis [48], but most importantly the strain and stress analysis was applied in orthopaedics, starting in the early 1970's [49].

5.2 - Formulation [50]-[52]

The FEM is characterized for modelling complex situations in discrete equations and points. From those defined solutions it is possible to interpolate any given point and obtain the chosen property. Therefore, this method allows for the accurate approximation, depending on the elements and the number of elements chosen, of a set of differential equations into discrete equation system in a finite number of points.

When FEA is applied to solid mechanics there are 4 main steps to follow:

- Mesh creation, and the elements forming it
- Formulation, where the node-dependent interpolation functions are defined

- Assembly, where the element-specific equations are combined
- Boundary conditions and external forces applications

After these steps are followed, the equations can be obtained for strain and stress, which are, in our case, the desired results.

For the first step, the physical domain is divided into elements, which are in turn interconnected through their nodes. The aggregate of the different elements and its nodes constitutes a mesh. In order to obtain a representative model of the chosen object, one must divide it into a certain number of elements (for orthopaedic members is usually of the order of thousands) while considering its computational costs.

The second stage of the finite element method requires that, for each element, the shape functions are defined. These shape functions should describe the element's behaviour and its variation across its structure and nodes.

Taking into consideration a determined u function, it can be represented through an approximated function u_h. This function will be defined as a linear combination of basic functions.

$$u \simeq u_h \tag{5.1}$$

$$u_h = \sum u_i \psi_i \tag{5.2}$$

ψ_i represents the basic functions and u_i the coefficients that approximate u_h to u. Figure 5.1 illustrates a 1D representation of the approximation of the u function. At any given point, the u_h function defined through the sum $\psi_i \times u_i$, as defined in equation (5.2). The basic functions will define how much impact a coefficient will have in determining the u_h function throughout the element. In the case described in figure 5.1, ψ_i is defined as linear basic functions where its value is 1 for the respective node and 0 in every other node. This is true for any shape function as well, what can alter are the values between the nodes. In figure 5.1, it is possible to observe how the problem can be represented if the nodes are uniformly distributed or not. An irregular node distribution can be applicable in cases where u has a greater variation, so it remains better represented in the u_h approximation.
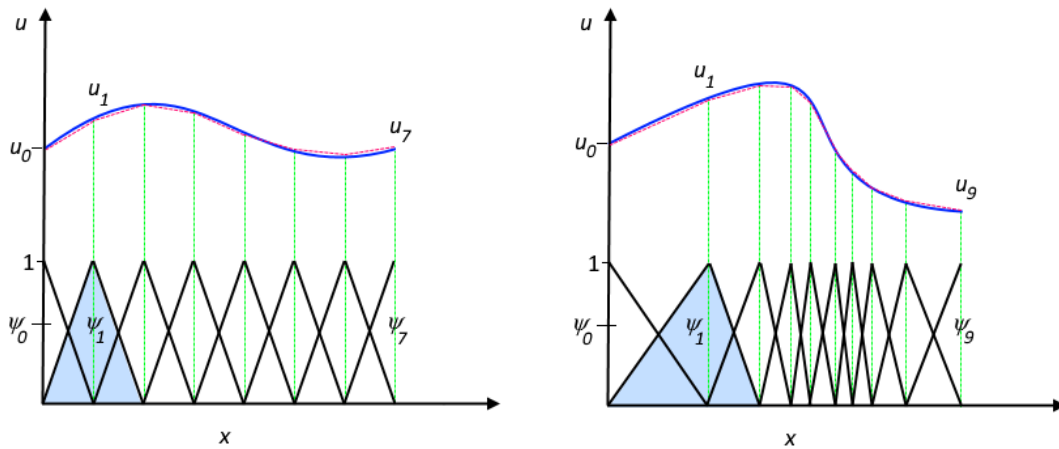
Figure 5.1 [53] - The function u, solid line blue, is approximated by u_h, dotted red line, which is calculated through a linear combination of ψ_i linear basis functions and the u_i coefficients. In the left a set of uniformly distributed is represented and in the right an irregular node distribution.

Considering a 2D finite element with n number of nodes, a vector of nodal displacements (in a 2D representation) is defined by:

$$\{\delta^e\} = \{u_1 \ v_1 \ u_2 \ v_2 \ \dots \ u_n \ v_n\} \tag{5.3}$$

For any given point in the element, the displacements can be calculated based on the nodal displacement vector $\{\delta^e\}$ and the element's shape functions, defined by N_i:

$$u = \sum N_i \, u_i \tag{5.4.1}$$

$$v = \sum N_i \, v_i \tag{5.4.2}$$

In a solid mechanics FEA problem the displacements caused by the applied loads are unknown. The known variables are the body geometry, the physical parameters and the applied loads, which in turn are transformed in forces applied to the nodes. To obtain the nodal displacements caused from these nodal forces, a relationship between them should be defined taking into account the geometry and the physical characteristics of the body. For each element, the potential energy state can be represented as π_e and its computation is represented in equation (5.5).

$$\pi_e = \frac{1}{2} \int_{V_e} [\delta_e]^T [B]^T DB \delta_e \, dV - \int_{V_e} [\delta_e]^T [N]^T p \, dV - \int_{S_e} [\delta_e]^T [N]^T q \, dS \tag{5.5}$$

In equation (5.5), δ_e represents the element's nodal displacements, N the shape functions, p the body forces per unit volume and q the applied surface tractions. Other unexplained variables will be explored in detail afterwards. For a system in equilibrium, the potential energy is minimum. To reach this minimum, the derivative of equation (5.5) in respect to the element's displacements, equation (5.6), should be equal to 0.

$$\frac{\partial \pi_e}{\partial \delta^e} = \int_{V_e} ([B]^T DB) \delta_e \, dV - \int_{V_e} [N]^T p \, dV - \int_{S_e} [N]^T q \, dS \tag{5.6}$$

This equation can be rewritten in a simpler manner when it is equated to 0, as is seen in equation (5.7).

$$F^e = K^e \, \delta^e \tag{5.7}$$

F^e represents the external forces applied in the nodes of the element, equation (5.8), and K^e denotes the element's stiffness matrix.

$$F^e = \int_{V_e} [N]^T p \, dV - \int_{S_e} [N]^T q \, dS \tag{5.8}$$

Having the nodal forces F^e determined as part of the conditions for the considered problem, it is still necessary to define the stiffness matrix of the element. It can be calculated through equation (5.9).

$$K^e = \int_V [B]^T D B dV \tag{5.9}$$

The stiffness matrix depends on two factors: one physical and other geometrical. The physical factors of the elements are introduced in the D matrix. This matrix is characterised by a 3×3 matrix, for 3D plane stress assumptions, that correlates local stresses with local strains through the Young's modulus (E) and the Poisson's coefficient (v). Both of these physical quantities are independent and experimentally obtained and depend solely of the material and its mechanical properties. To calculate the D matrix the equation (5.10) is used, applied for plane strain:

$$D = \begin{bmatrix} \dfrac{(1-v)E}{(1+v)(1-2v)} & \dfrac{vE}{(1+v)(1-2v)} & 0 \\ \dfrac{vE}{(1+v)(1-2v)} & \dfrac{(1-v)E}{(1+v)(1-2v)} & 0 \\ 0 & 0 & \dfrac{E}{2(1+v)} \end{bmatrix} \tag{5.10}$$

The B matrix incorporates the geometrical factors. This matrix relates the element's deformation with its nodal displacements. The calculation relies upon the shape functions N_i. This matrix will differ in size depending on the amount of nodes that the element has, having a $3 \times 2n$ size, considering a 2D element and n number of nodes. This matrix can be calculated through equation (5.11).

$$B = \begin{bmatrix} \dfrac{\partial N_i}{\partial x} & 0 \\ 0 & \dfrac{dN_i}{dy} \\ \dfrac{dN_i}{dy} & \dfrac{\partial N_i}{\partial x} \end{bmatrix}_{i=1,2,...,n} \tag{5.11}$$

As seen in equation (5.9), the FEM requires a volume integral. Depending on the element chosen this can be of varied levels of difficulty. For a linear element, the estimation of the integral should easily feasible. However, for a more complex element with curve lines, for example, the computation of the volume integral can become of severe difficulty. To ease this step, isoparametric elements are usually applied by defining the element in natural coordinates. The natural coordinate system is defined according to the element's geometry, making it simpler to work with the volume integral. Since the natural coordinates system do not vary according to the Cartesian geometry of the element, the element in its natural

coordinates will be represented in the same way regardless of its Cartesian geometry. In figure 5.2, a representation of the transformation of an element is presented in its natural coordinates.
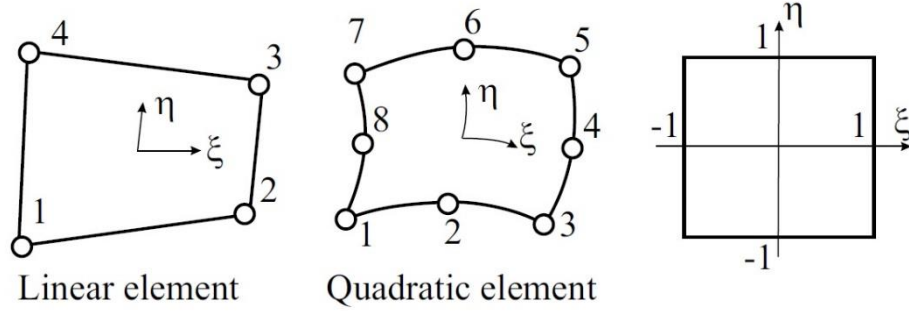
Figure 5.2 - Linear and quadratic elements represented in their Cartesian coordinates with the natural coordinates system superimposed over it and, in the right, the representation of both elements in their natural coordinates.

After the element is represented in its natural coordinates, it is necessary to define the shape functions according to this system. The way the shape functions are defined depends on the number of element nodes. Considering the example displayed in figure 5.2, the shape functions for a 4 node element can be define through equation (5.12) for all nodes, and the shape functions for an 8 node element can be defined through equations (5.13.1) to (5.13.3), considering that ξ and η represent the nodes' natural coordinates

$$Ni = \frac{1}{4}(1 + \xi)(1 + \eta) \tag{5.12}$$

$$Ni = \frac{1}{4}(1 + \xi)(1 + \eta) - \frac{1}{4}(1 - \xi^2)(1 + \eta) - \frac{1}{4}(1 + \xi)(1 - \eta^2), \\ i = 1, 3, 5, 7 \tag{5.13.1}$$

$$Ni = \frac{1}{2}(1 - \xi^2)(1 + \eta), \quad i = 2, 6 \tag{5.13.2}$$

$$Ni = \frac{1}{2}(1 + \xi)(1 - \eta^2), \quad i = 4, 8 \tag{5.13.3}$$

Consequently, the elements of the **B** matrix, which have to be obtained through derivatives of the Cartesian coordinates, can be obtained from the natural coordinates following equation (5.14).

$$\begin{Bmatrix} \dfrac{\partial Ni}{\partial x} \\ \dfrac{\partial Ni}{\partial y} \end{Bmatrix} = [J]^{-1} \begin{Bmatrix} \dfrac{\partial Ni}{\partial \xi} \\ \dfrac{\partial Ni}{\partial \eta} \end{Bmatrix} \tag{5.14}$$

The Jacobian matrix is defined by the equation (5.15), however, another way of obtaining it, through the data available is using equation (5.16).

$$J = \begin{bmatrix} \dfrac{\partial x}{\partial \xi} & \dfrac{\partial x}{\partial \eta} \\ \dfrac{\partial y}{\partial \xi} & \dfrac{\partial y}{\partial \eta} \end{bmatrix} \tag{5.15}$$

$$\frac{\partial x}{\partial \xi} = \sum \frac{\partial Ni}{\partial \xi} x_i , \quad \frac{\partial x}{\partial \eta} = \sum \frac{\partial Ni}{\partial \eta} x_i$$
$$\frac{\partial y}{\partial \xi} = \sum \frac{\partial Ni}{\partial \xi} y_i , \quad \frac{\partial y}{\partial \eta} = \sum \frac{\partial Ni}{\partial \eta} y_i \tag{5.16}$$

With this method the derived shape functions can be easily transformed from their natural coordinates to their Cartesian coordinates, which allows for the construction of the B matrix presented in equation (5.11).

Taking into account that the FEM is an approximation method, the computation of the volume integral for K^e is a complex operation that can be simplified by using the Gauss-Legendre quadrature. In this work, only triangular elements will be used and its application to this method will be explained through that point of view.

For this approximation method, integration points are defined inside the element where the integration values are calculated and to each point a weight is attributed. The number of integration points can vary, but with that change, so does the weight of each point. In figure 5.3, examples of a different number of integration points, applied to triangular elements, are presented. In table 5.1, the natural coordinates of each integration point, and the corresponding weight assigned to each point, are shown.

(a) 1 Integration Point   (b) 3 Integration Points   (c) 4 Integration Points
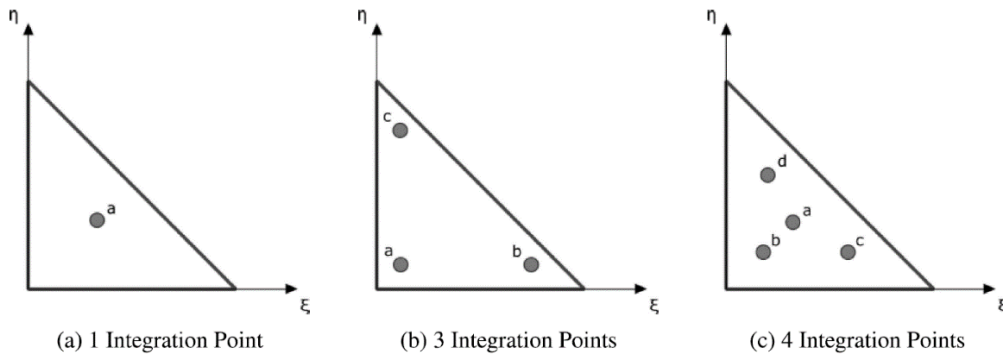
Figure 5.3 [52] – Gaussian-Legendre quadrature applied on a triangular element with (a) 1 integration point, (b) 3 integration points and (c) 4 integration points

Element	Points	ξ	η	Weight
(a)	a	$\dfrac{1}{3}$	$\dfrac{1}{3}$	$\dfrac{1}{2}$
(b)	a	$\dfrac{1}{6}$	$\dfrac{1}{6}$	$\dfrac{1}{6}$
	b	$\dfrac{2}{3}$	$\dfrac{1}{6}$	$\dfrac{1}{6}$
	c	$\dfrac{1}{6}$	$\dfrac{2}{3}$	$\dfrac{1}{6}$
(c)	a	$\dfrac{1}{3}$	$\dfrac{1}{3}$	$-\dfrac{27}{96}$
	b	$\dfrac{1}{5}$	$\dfrac{1}{5}$	$\dfrac{25}{96}$
	c	$\dfrac{3}{5}$	$\dfrac{1}{5}$	$\dfrac{25}{96}$
	d	$\dfrac{1}{5}$	$\dfrac{3}{5}$	$\dfrac{25}{96}$

Table 5.1 – Gaussian-Legendre quadrature applied on a triangular element with (a) 1 integration point, (b) 3 integration points and (c) 4 integration points

From this the complex volume integral can be replaced by a more simple calculation, using the right-hand side of the equation (5.17), being w_i the weight of the corresponding integration point

$$dV = \partial x \partial y = \det(\boldsymbol{J}) \, \partial \xi \partial \eta = \det(\boldsymbol{J}) \, w_i \tag{5.17}$$

The final computation for the stiffness matrix will then be represented by the equation (5.18).

$$\boldsymbol{K}^e = [\boldsymbol{B}]^T \, \boldsymbol{D} \, \boldsymbol{B} \, \det(\boldsymbol{J}) \, w_i \tag{5.18}$$

After $\boldsymbol{K}^e$ is determined for each element, the assembly of elements' matrices is performed and a global stiffness matrix is created, containing the values from the elements' specific stiffness matrix. It is important to note that for overlapped nodes, in the global stiffness matrix, the values must be added. In figure 5.4 is presented a 1D bar divided into 3 elements, each with 3 nodes, where some of the nodes belong to more than one element.
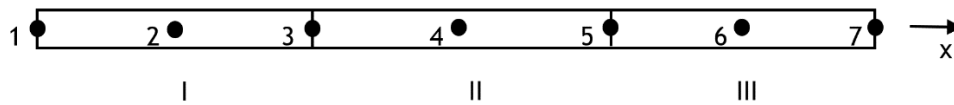
Figure 5.4 [50] – 1D bar with 3 different elements (I, II, and III) each with 3 nodes, 2 of them overlapping different elements

Each element has a stiffness matrix associated, represented in equations from (5.19.1) to (5.19.3). When the global matrix is generated, the assembly process must follow the procedure portrayed in equation (5.20).

$$\boldsymbol{K^I} = \begin{bmatrix} a_{11} & a_{12} & a_{13} \\ a_{21} & a_{22} & a_{23} \\ a_{31} & a_{32} & a_{33} \end{bmatrix} \tag{5.19.1}$$

$$\boldsymbol{K^{II}} = \begin{bmatrix} b_{11} & b_{12} & b_{13} \\ b_{21} & b_{22} & b_{23} \\ b_{31} & b_{32} & b_{33} \end{bmatrix} \tag{5.19.2}$$

$$\boldsymbol{K^{III}} = \begin{bmatrix} c_{11} & c_{12} & c_{13} \\ c_{21} & c_{22} & c_{23} \\ c_{31} & c_{32} & c_{33} \end{bmatrix} \tag{5.19.3}$$

$$\boldsymbol{K} = \begin{bmatrix} a_{11} & a_{12} & a_{13} & 0 & 0 & 0 & 0 \\ a_{21} & a_{22} & a_{23} & 0 & 0 & 0 & 0 \\ a_{31} & a_{32} & a_{33}+b_{11} & b_{12} & b_{13} & 0 & 0 \\ 0 & 0 & b_{21} & b_{22} & b_{23} & 0 & 0 \\ 0 & 0 & b_{31} & b_{32} & b_{33}+c_{11} & c_{12} & c_{13} \\ 0 & 0 & 0 & 0 & c_{21} & c_{22} & c_{23} \\ 0 & 0 & 0 & 0 & c_{31} & c_{32} & c_{33} \end{bmatrix} \tag{5.20}$$

After the assembly of the global stiffness matrix is performed, the essential boundary conditions (displacement constrains) and natural boundary conditions (external forces) must be defined. The essential boundary conditions are imposed using the Penalty Method. The term to be constrained, corresponding to the specific node and direction, is penalized by multiplying that term by a constant α which should be a large enough number, usually $E \times 10^{32}$. This penalty method is also applied to the force vector, in the same directions applied in the stiffness matrix, exemplified in equation (5.21).

$$F_i^{pen} = \begin{cases} \alpha K_{ii}\,\bar{u}_i, & if\ it\ is\ penalized \\ F_i, & otherwise \end{cases} \tag{5.21}$$

From the penalized stiffness matrix, $\boldsymbol{K^{pen}}$, and the penalized force vector, $\boldsymbol{F^{pen}}$, the displacement vector, δ, is obtained through equation (5.22).

$$\delta = [\boldsymbol{K^{pen}}]^{-1}\,\boldsymbol{F^{pen}} \tag{5.22}$$

Using equation (5.23), the reaction forces vector, $\boldsymbol{F^R}$, are obtained by using the unpenalized stiffness matrix, equation (5.20), and the displacement vector. Through equation (5.24), the strain values, ε, are calculated and with equation (5.25), the stress values, σ, are computed.

$$\boldsymbol{F^R} = \boldsymbol{K}\,\delta \tag{5.23}$$

$$\varepsilon = \boldsymbol{B}\,\delta \tag{5.24}$$

$$\sigma = \boldsymbol{D}\,\varepsilon \tag{5.25}$$

Using the demonstrated equations, the Finite Element Method is used in order to perform the mechanical analysis, concluding with the determination of the stress and strain, shown in last two equations presented.

34

Chapter 6

Finite Element Method in Orthopaedics

6.1 - The start

As mentioned in the previous chapter, FEM in its early stages showed to have several applications and one of those examples was in orthopaedics. The seminal article on the topic was Brekelmans' paper, which proposed a new mathematical model to better study the mechanical behaviour of skeletal parts [54]. With this paper, Brekelmans proved that FEA was far superior to the existing mathematical and experimental techniques. In this article, Brekelmans studied an entire femur and found that forces applied from the abductor muscles substantially determined mid-diaphyseal stresses.

6.2 - The first decade

The early developments of FEM in orthopaedics is accurately described in a review paper written by Huiskes and Chao [55]. In it, it is stated that since the discovery of the application of FEA, this method was considered as a magical tool to all problems without the necessary capabilities and knowledge of its limitations [55]. What allowed for the growth of FEA was the thorough method-oriented work that was developed in order to enhance this method of analysis. In the great majority of these, a study of the femur is performed since, besides being the longest bone in the body, it has historical developments and it is commonly involved in orthopaedic treatments, one of those being the prosthetic replacement of the hip joint.

After the 2D model proposed by Brekelmans, several articles arose proposing 3D models in order to compare results between 2D and 3D models. Articles such as Scholten's [56] and Olofsson's [57], proved that FEA was effective for 3D analyses despite demanding a more rigorous analysis with more sophisticated models; Scholten's model was an exceptionally refined one, with a mesh density allowing as much as 10,000 degrees of freedom, approximately.

Work in a problem-oriented point of view began to be developed few years later and it can be divided into three categories, in which only the first two will be focused here: stress analyses of bones, artificial joint design and fixation and fracture of bones.

From the first category, several articles focused on the mechanical properties in different bones or regions of the same bone. For example, Brown and Ferguson, in 1978, built a 2D model of a femoral head, which included trabecular bone in order to study its influence on the femur's mechanical properties [58]. However, it considered that the bone was formed by a continuous material, just with different mechanical properties. Hayes et al., in an ongoing study, developed a study to investigate bone growth and remodelling. Using a 2D FE model, it was found that high Von Mises effective stress correlates with regions of high trabecular density [58],[59].

Since orthopaedics requires heavy use of prosthetics, it is also important to focus on some research work dealing with that topic. The first works on this subject consisted of 2D models for total hip replacement (THR). Articles published by Andriacchi et al. [61], Kwak et al. [62] and Sih et al. [63] reported on several different prosthesis, varying in size and geometry, with distinct loadings applied. This divergence made it impossible to compare the different studies in a quantitative sense. 3D models of the same prosthesis were later on developed by studies such as Roehrle et al. [64], Valliapan et al. [65] and Lewis et al. [66]. For the same reasons as the aforementioned, no quantitative comparison was able to be performed. Studies started to investigate further into problems related to artificial joints. On articles submitted by Anand et al. [67] and Ducheyne et al. [68], the influences of bone ingrowth in porous coatings was studied with the conclusion that the value of the elastic modulus of the porous coating has no major influence on the interfacial shear stress occurring in the porous coating spongy bone (upon compression and bending). Lastly, analysis on the acetabular cup were also performed using FEA, both in 2D models – Vasu et al. [69] and Carter et al. [70] – and 3D models – Oonishi et al. [71] and Goel et al. [72].

6.3 - Problem-oriented development

From the earliest developments, it was obvious that when applied correctly FEA was extremely helpful in orthopaedics. After its initial exploration and progress, largely due to the method-oriented work developed, the work leaned increasingly more towards the application the FEM could have in this field. In a reputed review article published by Prendergast [73], the author reports on the great achievements carried out by FEA studies on biomechanics until 1997. In it, Prendergast splits the bibliography in three different groups: the FEM applied to skeletal parts, the FEM applied to prosthesis and other orthopaedic devices and the FEM applied in tissue adaptation studies.

In the studies regarding FEA applied to skeletal parts, several analyses stand out. Hogan [74] studied the effect of microcracking in bone. In it, the conclusion was reached that the predicted variation in the elastic modulus with porosity was observed, however not as sensitive as observed experimentally. A big step was taken with Beaupré's article [75], in which the first 3D model of trabecular bone was built with its trabecular architecture. Brown and Hild [76], in 1983, used a 3D model of a femoral head to prove that development of osteonecrosis causes stress increase which predisposes a mechanical collapse of the femoral head. And lastly, in 1991, Lotz [77] showed that the von Mises stress best predicts a fracture site of the femoral bone.

Regarding the FEM applied to prosthesis and more orthopaedics devices, several projects worked on different angles approaching the same global problem. In 1983, Rohlmann et al. [78]

presented the first large 3D model of hip replacement, calculating stresses in the prosthesis, cement and bone showing the effect of musculature. Several different parts of hip prosthesis were evaluated in distinct articles. In Fagan's [79] and Prendergast's [80] work, the effect of a collar on the prosthesis stem was evaluated, with the conclusion that the structure can create more physiological calcar stress if it remains in contact with the excised surface. Little et al. [81] used a 2D finite element model of the medial plateau, cement and bone to establish suitable sites for implantation 3D strain gauges. In a particularly relevant paper, Huiskes and Vroemen [82] introduced the concept of preclinical evaluation by predicting maximum normal and shear stresses at the interfaces of prostheses with different designs.

Equally important was the work developed on tissue adaptation when FEA was applied. As regards to this particular field, one paper stands out. Huiskes et al. [83] studied the interface stresses increase and remodelling rate decreases with a decreasing Young's modulus of the prosthesis.

It is also important to mention that with the state of development at the time, researchers had some concerns. For instances, Viceconti et al. [84] suggested that an over-emphasis on visual similarity of the model and reality has occurred because clinicians are trained to rely on observation rather than modelling, which can hinder the results obtained.

6.4 - Recent developments

In recent years, FEA has been used as a patient-specific tool with different objectives. With the latest evolution of faster computers and more advanced imaging modalities, the possibility of producing a model that closely represents the bones of an individual person is well within reach. Whether it is to perform a simple stress analysis of bone, evaluate an injury or analyse prosthesis conditions, this technique is very useful for orthopaedists and surgeons by providing extra information allowing the medical doctor to perform a better informed analysis.

There are two main approaches to obtain a patient-specific model.

In the first, one makes use of current imaging models to obtain a base image where, using image segmentation, it is possible to outline the bone. Afterwards, a FE mesh is created on the bone outlined. To assert the mechanical properties, a two-step procedure is conducted: firstly, the literature for the core values is assessed and after, correlating with the grey level of the image, the mechanical values are attributed accordingly. After associating the loading and boundary conditions, FEA can be performed to assess stress and strain.

For the second approach, a statistical shape intensity model (SSIM) can be built. For it, the model is built considering a population of bones and simply requires a 2D image to generate a 3D model. This technique has several advantages, starting from simpler image acquisition to allowing for more complex calculations. However, it is still in early stages of development with not a lot of work performed with it [85].

Recent work has shown the versatility of FEM. Little et al. [86] studied bone stress distribution using a patient-specific model while Abdul-Kadir et al. [87] studied how interference fit could affect implant micromotion. In addition, when combined with quantitative image modalities, such as qCT, FEA can provide supplementary information which can enhance interpretation of data [85]. This is proven with articles written by Cody et al. [88] and Tanck et al. [89] where both authors concluded that FEA produced better results than quantitative image modalities, as qCT and DXA.

What comes to light, however, is the majority of work developed with patient-specific FE models resorting to high end image modalities, such as CT or MRI, to create a 3D model. However, as mentioned in the first chapter, these imaging modalities are not as frequently used as radiographs. With that said, the project to be developed aims to correct that shortcoming using X-ray radiographs to produce 2D FE models.

Chapter 7

Femur Analysis Tool

7.1 - Introduction

Trying to answer the needs previously presented, the project to develop the Femur Analysis Tool was started. With this, the goal was to create a tool that, using single femur X-ray radiographs, would be able to segment the femoral bone generating a computational femur model. From this model, a mesh is created, allowing to perform a qualitative FEM analysis and understand the structural influence of the applied external forces.

Despite the existence of a wide variety of published articles showing an interest in the research of the propagation of stress and its effects on bone (several examples have been discussed before in chapter 6), few commercial solutions have been found that can apply this knowledge to the clinical practice. One software developed by the Computational Mechanics Laboratory – CMECH-Lab (cmech.webs.com), Tool, was able to perform this mechanical analysis [90]. However, it required the physician to manually trace the model of the femur, making use of reference points. With the Femur Analysis Tool, herein presented, the goal is to have the process as automatized as possible, including the creation of the femoral head.

7.2 - Software Workflow

This software follows the workflow presented in figure 7.1.
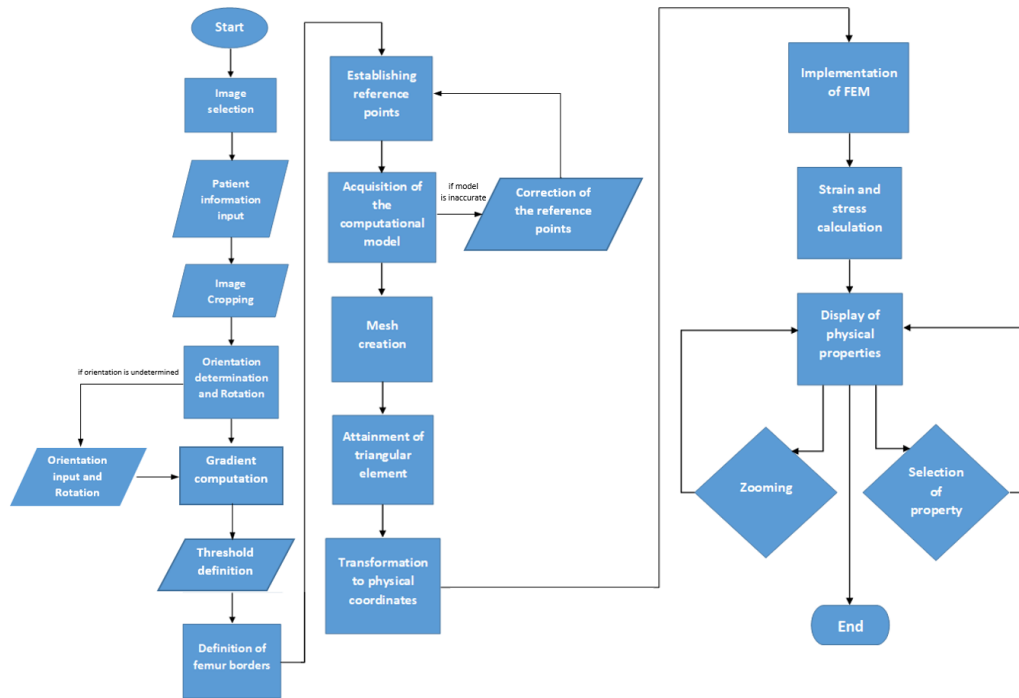
Figure 7.1 – Femur Analysis Tool workflow

The developed software starts by requiring an image input of a femur X-ray radiograph. After that step, the user has to input information regarding the patient, namely the patient's age, height, weight and gender, followed by a step in which the user can crop the image (if the radiograph doesn't have the appropriate content). Afterwards, the algorithm itself runs starting by determining the orientation in which the femur is presented, rotating it, if needed. This operation is required so that the femoral head is pointing towards the top right corner. If that orientation is undetermined, the user selects the orientation. From the rotated image, the horizontal and vertical gradients are computed and subsequently thresholded. The threshold is defined by the user in order to obtain a clearer binary image. These gradients aid the detection of the borders of the femur which is the next step. From these borders, some reference points are established and these said points will guide the creation of the femoral model. If the femoral model provided by the software has some inaccuracies, the next step allows for the correction of the reference points which leads to a new and improved computational model. The following step, mesh creation, sets the nodes for the femoral model and from these nodes, triangular elements will be generated. The images coordinates are transformed into physical coordinates, a valuable step to ensure the correct values are calculated further on. From then on, the FEM is applied and all the nodes' and elements' properties and matrices are computed. This allows for the strain and stress for each element to be calculated and, from this result, related physical quantities are displayed. The user then has the choice to zoom in to see the result in intended regions, affecting the display at hand or select a different property to be displayed.

These are the main activities carried out by the software. However, for each step several subtasks are being performed by the algorithm. Such subtasks will be described in the following subchapters.

7.3 - Software Algorithm

7.3.1 - Determining the image orientation

As previously mentioned, the standard chosen orientation for the femur radiograph contains the femoral head pointing towards the top right corner. To assess the orientation of the radiograph, the weighted average centre of intensity of the image is calculated, following equation (7.1), in which IC represents the calculated centre of intensity, x is the x coordinate for each iteration, y the y coordinate and $i(x,y)$ corresponds to the pixel intensity for coordinates x and y.

$$IC = \left(\frac{\sum(x \cdot i(x,y))}{\sum i(x,y)}, \frac{\sum(y \cdot i(x,y))}{\sum i(x,y)} \right) \qquad (7.1)$$

From this equation, it is possible to calculate where the centre of intensity of the image is located. The expected result, if the femoral head is aiming towards the top right corner, should show the centre of intensity in the first quadrant of the image – the top-right one. This happens due to the presence of the hip in the image. As it is a voluminous bone and with great thickness, it pulls the centre of intensity towards its position, which is correspondent to the position of the femoral head. For this determination, to avoid noisy images, a window of 10% of width and height was set in which if the centre of intensity was placed within 10% of each image dimension from the centre of the image the user determines the orientation of the image.

After this orientation is set, the image is then flipped accordingly, or not, to match the desired orientation. If the centre of intensity falls on top right corner, nothing happens. However, if the centre of gravity falls on the top left corner, the image is flipped horizontally, if it falls on the bottom right corner, the image is flipped vertically and if the centre of gravity is placed on the bottom left corner, the image is flipped both horizontally and vertically.

(a)   (b)
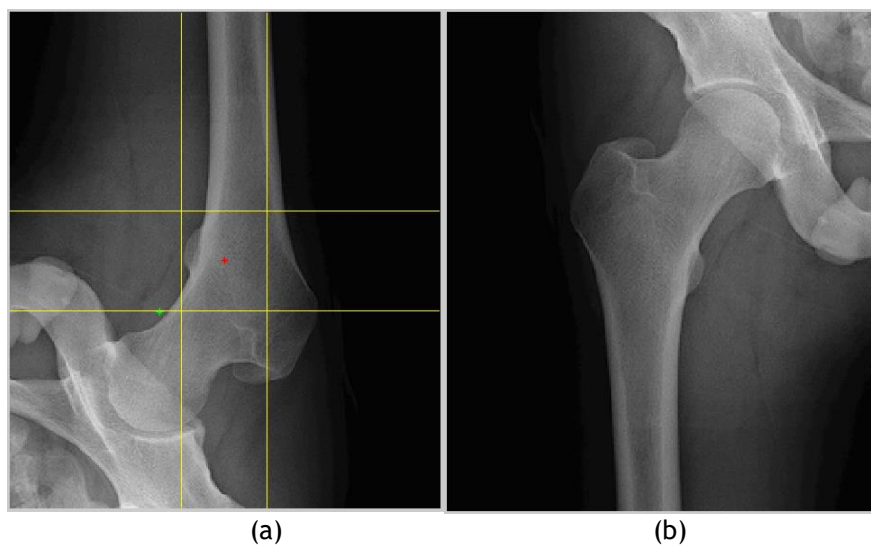
Figure 7.2 – (a) Femur radiograph displaying the centre of the image (red dot) and the intensity centre (green dot) with the 10% window (yellow lines) (b) Femur radiograph after the appropriate flipping

In figure 7.2, this is represented where in figure 7.2a the centre of intensity is detected in the bottom left quadrant of the image and therefore requires a horizontal and vertical flip to obtain figure 7.2b.

7.3.2 - Gradient computation and thresholding

Prior to calculating the gradients, the image is pre-processed. This step was performed in order to better mimic the test conditions. Therefore, the average pixel intensity was calculated and its difference to 0.23 was subtracted to all pixels, as demonstrated in equations (7.2) to (7.4). avg represents the average intensity of the image, $i(x_i, y_i)$ represents the intensity of a pixel with coordinates (x_i, y_i), $diff$ stands for the difference between

$$avg = \frac{\sum_{i=1}^{N} i(x_i, y_i)}{N} \tag{7.2}$$

$$diff = avg - 0.23 \tag{7.3}$$

$$i(x_i, y_i) = i(x_i, y_i) - diff \tag{7.4}$$

It is important to note that in equation (7.4) any value below 0 is automatically adjusted to 0.

Following the decrease of luminosity of the image, a contrast adjustment is performed. To perform this step, the intensities are rescaled to occupy the full range of intensities, from 0 to 1. To execute this, the maximum and minimum intensities are calculated and a linear correlation between the current intensities and the contrast-enhanced ones was established using equations (7.5) and (7.6). In equation (7.7), the contrast adjustment step is performed. For these equations, max represents the maximum intensity of the image while min represents the minimum intensity of the image. m represents the slope of the linear correlation and b describes the intersection of the linear regression with x=0.

$$m = \frac{1 - 0}{max - min} \tag{7.5}$$

$$b = 0 - m \cdot min \tag{7.6}$$

$$i(x_i, y_i) = m \cdot i(x_i, y_i) + b \tag{7.7}$$

The result of these transformations can be seen in figure 7.3.

(a)   (b)
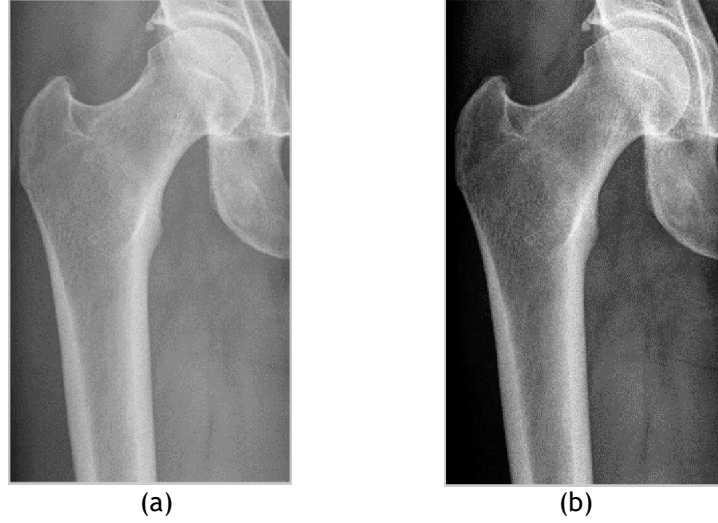
Figure 7.3 – (a) Original femur radiograph (b) Femur radiograph after pre-processing steps of brightness decrease and contrast adjustment

After the image has the suitable orientation, the gradient is computed to aid with the detection of the femur borders. This is possible due to the characteristics of the femoral radiographs. Since the foreground of the femur is much brighter than the surrounding background, by calculating the horizontal and vertical gradient we can define the borders for the femoral bone. To compute the vertical and horizontal gradient, equations (7.8) and (7.9) were used, respectively.

$$g_V(x,y) = \begin{cases} i(x,2) - i(x,1), & if \ y = 1 \\ \frac{1}{2} \cdot \big(i(x,y+1) - i(x,y-1)\big), & if \ y \neq 1 \vee y \neq y_N \\ i(x,N) - i(x,N-1), & if \ y = y_N \end{cases} \qquad (7.8)$$

$$g_H(x,y) = \begin{cases} i(2,y) - i(1,y), & if \ x = 1 \\ \frac{1}{2} \cdot \big(i(x+1,y) - i(x-1,y)\big), & if \ x \neq 1 \vee x \neq x_N \\ i(N,y) - i(N-1,y), & if \ x = x_N \end{cases} \qquad (7.9)$$

From this gradient calculation, an enhancement is applied, shown in equations (7.10) and (7.11).

$$g_H enhanced(x,y) = (200 \cdot g_H(x,y))^3 \qquad (7.10)$$

$$g_V enhanced(x,y) = (50 \cdot g_V(x,y))^3 \qquad (7.11)$$

The values for the enhancement were determined by a trial and error method. However, the goal was to enhance bigger values of the gradients and, therefore, using a cubic function guarantees these higher values will be enhanced, while smaller values are not.

Following the enhancement step, the gradients are thresholded to create binary images. The thresholds are determined by the user using the provided interface, in a step explained

further on. For now however, the thresholds will be defined as t_h for the horizontal threshold and t_v for the vertical threshold. The enhanced horizontal gradient is then thresholded at t_h and also at $-t_h$. While the first threshold allows for the detection of dark-to-white transitions, the second threshold detects the opposite white-to-dark transitions. The enhanced vertical gradient, on the other hand, has its absolute value thresholded at t_v. For the vertical gradient, the information of which transition occurs is not so relevant, hence, the absolute value is thresholded instead of the signed value.

This step is followed by a verification of meaningful or non-meaningful points. To achieve this, the neighbourhood of each positive pixel is verified. If the positive pixel does not have two other positive pixels within a distance of 2 pixels, the point is ruled out. The resultant binary image can be seen in figure 7.4b.

(a)   (b)
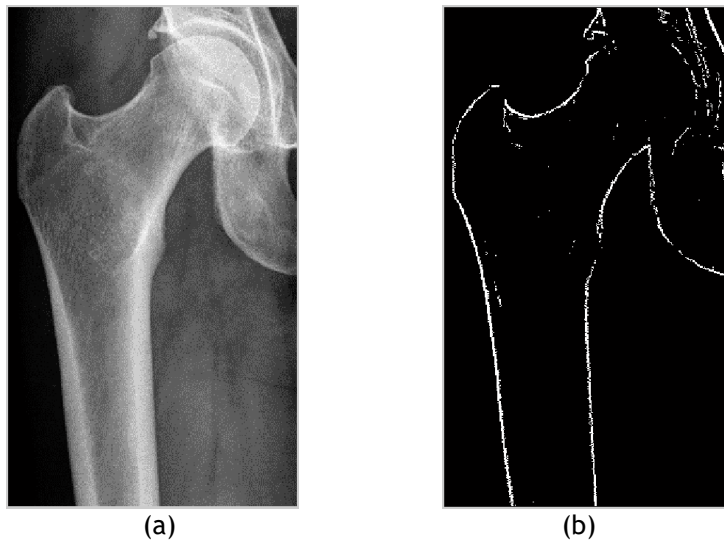
Figure 7.4 – (a) Femur radiograph with contrast adjustment (b) Binary image with the union of thresholded points for the horizontal and vertical gradient

In figure 7.4b, despite presenting some noise regarding the pelvis and the inner structure of the femur, it is clearly seen the borders of the femur well defined. From this image a model for the femur can be generated.

7.3.3 – Defining the femoral head

The detection of the femoral shaft is intuitive when the gradient is well defined, however a region that takes more time to be found is the femoral head.

Since the femoral head is placed in the acetabulum, which has all the other pelvis' structures surrounding it, this requires an intricate algorithm to detect the position of the femoral head. To perform this, some relationships between the femur's structures, mentioned before in chapter 2, are taken into consideration. The two relationships used in this work are: the angle between the shaft and the neck is, in average, 135º [7], and the highest point of the great trochanter has the same height as the centre of the femoral head [7]. Having both structures defined, the intersection of these conditions gives an approximate location of the centre of the femoral head.
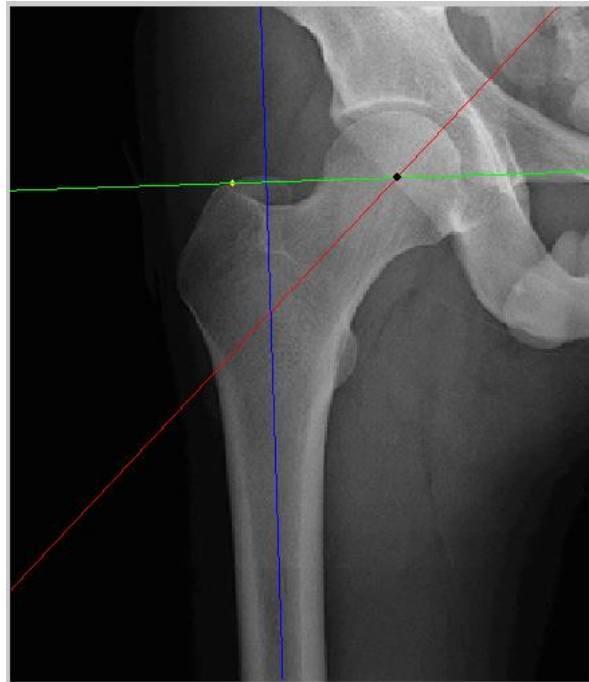
Figure 7.5 – Femur radiograph demonstrating the relationships between the femoral inner structures with the femoral shaft axis (blue line), the neck axis (red line), the highest detected point of the greater trochanter (yellow point) and the perpendicular line to the shaft axis (green line). The intersection of the perpendicular line to the shaft axis and the neck axis determines the head centre (black point)

As it is seen from figure 7.5, the intersection between the two mentioned relationships allow for the approximate detection of the femoral head centre.

Delving deeper in this process, the shaft axis is determined since the knowledge of the borders of the shaft is obtained from the gradient image. From the same image, the femoral neck borders are retrieved. The two closest opposing points in the femoral neck warrants the definition of the neck midpoint. With the neck-shaft angle – 135° - and the defined neck midpoint, the neck axis can be determined. In this figure, it is perceivable that the trochanter highest point established is not correct, as the greater trochanter projects itself to the back and that portion of the structure achieves a greater height. However, the difference is not significant since the neck axis can also vary slightly. It is important to note that to make out the height of which the centre of the femoral head should have, stipulated by the green line, we should look at the perpendicular of the femoral shaft axis since the inclination of both the bone and also the scan itself can heavily impact that measurement.

From this approximate head centre, a window 50x50 pixels is set around the set head centre. A range of radii is set around a relationship found by Kazemi et al. [91]. In this work it was found that the ratio between the femoral head diameter and the femoral neck diameter is averaged at 1.33. Hence, the neck diameter was averaged out and a mean head diameter was calculated. Halving this diameter the range of radii was set from the average radius minus 5 pixels to the average radius plus 5 pixels with 0.2 pixels as the step. From these ranges of possible head centres and radii, an iterative process was carried out. In each iteration, the resulting circumference verified for the presence of positive pixels regarding the binary thresholded image obtained previously. For each pixel found, a point would be added to its score. In the end of the iterative process, the circumference with the highest score would be

selected and consequently its centre and radius was saved. The result can be seen in figure 7.6.

Figure 7.6 – Femur radiograph with the selected head centre and the circumference resulting in the femoral head

7.3.4 - Establishing the reference points and defining the model

From the defined borders, reference points are defined. These points are exhibited in figure 7.7

Figure 7.7 – Reference points displayed on the femoral radiograph labelled with an identifying letter

The aforementioned points will help define the femoral model. Six points, three for each border, will define the shaft – points A, B, C, O, P and Q in figure 7.7. Point E is defined as the most left point in the greater trochanter. Point F, on the other hand, is defined as the top point of the greater trochanter. Point G is characterized by its lowest y coordinate on the top border. Points H and M are determined by being the opposing points in the femoral neck with the lowest distance between them. Points J and K determine the diametrically opposite points in the femoral semi-circle. The remaining points, points D, I, L and N, serve as auxiliary points to fit the model to the true shape of the femur.

These reference points act as guides to outline the femur model. In the shaft, a straight line is determined between consecutive points. Since the curvature is negligible, the approximation of the shaft to a pair of polygons does not cause a significant error. Between points J and K, a semicircle will define the femoral head. Also, between points E and F a straight line is also determined, for the same reasons as mentioned previously – low curvature between these two points. Between the remaining points, however, a spline curve must be defined to follow the border of the femur. The result generates a model that can be seen in figure 7.8.

Figure 7.8 – Femoral model (blue line) represented on top of the femur radiograph

The process of generation of spline curves will be explained in the following subchapter.

7.3.5 - Spline curves

To compute the spline curves needed for the femur model, the cubic spline interpolation method is applied. Given some reference points, the cubic spline interpolation method creates a polynomial curve up to the third degree which best fits the reference points given. In this subchapter, a simple explanation of cubic spline interpolation will be given as a starting point for the algorithm applied to obtain the spline curves.

Given n number of points, $n-1$ curves are created between these points. An example is shown in figure 7.9.
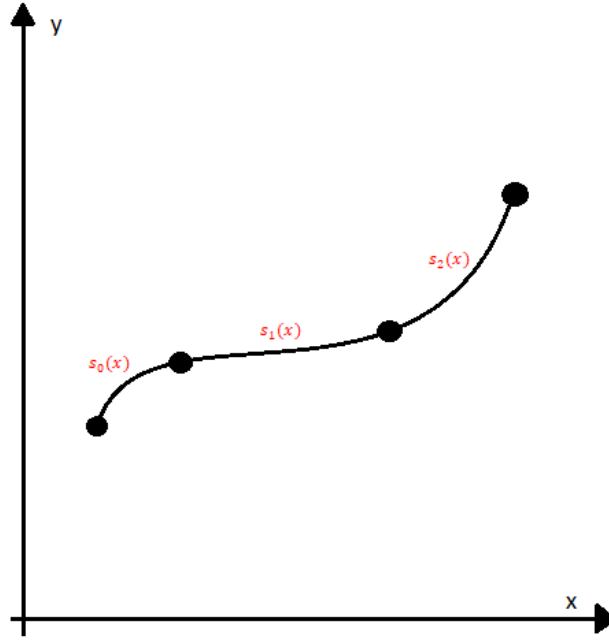
Figure 7.9 – Example of spline curve between 4 points

Between each point the equation of a curve is defined, which is represented in its general coefficients in equations (7.12) to (7.14).

$$s_0(x) = a_0 + b_0(x - x_0) + c_0(x - x_0)^2 + d_0(x - x_0)^3 \tag{7.12}$$

$$s_1(x) = a_1 + b_1(x - x_1) + c_1(x - x_1)^2 + d_1(x - x_1)^3 \tag{7.13}$$

$$s_2(x) = a_2 + b_2(x - x_2) + c_2(x - x_2)^2 + d_2(x - x_2)^3 \tag{7.14}$$

The coordinates of each point are known, the unknown variables in these equations are the coefficients of the equation for each curve. In this case we have 12 unknown variables, and therefore we need 12 equations that can give us the solution. To get these values there are several conditions that need to be computed and these conditions will be outlined here.

For each curve, the starting point is known and for the last curve, the finishing point is known. Therefore, it is possible to determine equations (7.15) to (7.18)

$$s_0(x_0) = y_0 \tag{7.15}$$

$$s_1(x_1) = y_1 \tag{7.16}$$

$$s_2(x_2) = y_2 \tag{7.17}$$

$$s_2(x_3) = y_3 \tag{7.18}$$

Between each curve, there is also an equality in the point that separates both curves. In those, matching conditions which are represented in equations (7.19) to (7.20), it is achieved,

$$s_0(x_1) = s_1(x_1) \tag{7.19}$$

$$s_1(x_2) = s_2(x_2) \tag{7.20}$$

So far, there are a total of 6 equations for 12 unknown variables, meaning there still needs to be 6 conditions to be uncovered.

Between consecutive curves, the transition should be smooth. In mathematical terms smoothness, this is defined by equating the first and second derivative of both curves. These relations are presented in equations (7.21) to (7.24).

$$s_0{}'(x_1) = s_1{}'(x_1) \tag{7.21}$$

$$s_1{}'(x_2) = s_2{}'(x_2) \tag{7.22}$$

$$s_0{}''(x_1) = s_1{}''(x_1) \tag{7.23}$$

$$s_1{}''(x_2) = s_2{}''(x_2) \tag{7.24}$$

In both ends boundary conditions can also be defined. In this case, and in the example applied in the algorithm, the ends are defined as a natural boundary. To follow this condition equations (7.25) to (7.26) are applied, which determine the last two equations required to obtain the coefficients.

$$s_0{}''(x_0) = 0 \tag{7.25}$$

$$s_2{}''(x_3) = 0 \tag{7.26}$$

The computation of set of equations (7.15) to (7.26) will determine the coefficients of the curves shown in the example.

The number of coefficients will vary depending on the number of points defining the spline curve. However, in the same amount, the number of conditions can be defined making the problem solvable.

Regarding the computational femoral model, three separate spline curves were computed, each one having different curves between each consecutive point. Resorting to figure 7.7, one spline curve was defined from points C to E, another between point F and point J, and the last one from point K to point O. Using the method described before with the same conditions, the algorithm is able to determine the coefficients for the spline curves and defining it so that the model is complete.

7.3.6 - Mesh creation

Following the determination of the femur computational model a node mesh is defined by the algorithm. After an input by the user determines the density of the mesh, the first patch to be populated is the femoral head patch. The head's semicircle is divided into radial divisions and circumferential ones. However, to maintain the mesh density, a linear regression is done between the perimeter of each radial division to calculate how many circumferential divisions should be performed. From this starting patch, the entire model is populated with nodes always

aiming to maintain the node density using the same linear regression applied to the femoral semicircle. The other remaining patches follow the same principle. First the number of divisions in each longitudinal border is defined and, after that, the inside of the patch is populated with nodes, building the resultant mesh.

The complete nodal mesh can be seen in figure 7.10.

Figure 7.10 – Nodal mesh displayed of the femoral computational model

7.3.7 - Triangular elements

The step following the nodal mesh creation is the formation of the triangular elements that are established using the created nodes. To perform this, the MATLAB function `delaunay` is used.

This function creates triangles between a set of points assuring no other points are inside each triangle. Despite the function's utility, it still generates unwanted elements. To rule out the undesired elements, two verification methods were applied.

For the first one, each element's angles were analysed. Even though the triangular elements inside the model are not perfectly equilateral, their angles don't have exceedingly high or exceedingly low values. This is not true for the elements formed outside the model. Therefore

the first verification method is represented in equation (7.27) and it was applied to all three angles in each triangular element.

$$angle > \frac{\pi}{9} \wedge angle < \pi - \frac{\pi}{9} \tag{7.27}$$

The second verification method relates to the element's area. Since the nodal mesh density is approximately constant throughout the model, the elements' area should be relatively equal through the model. This, however, fails to occur in elements appearing outside the element in which they have either an incredibly large area or incredibly small. To rule out the elements outside the model, the area is calculated for every element. After that, the average and standard deviation is computed and the verification method is applied using equation (7.28), in which avg_{area} represents the average, std_{area} describes the standard deviation and $area$ relates to each element's area.

$$area > avg_{area} - 2 \cdot std_{area} \wedge area < avg_{area} + 2 \cdot std_{area} \tag{7.28}$$

In figure 7.11 the elements generated are represented, both before and after the verification methods are applied.

(a)   (b)
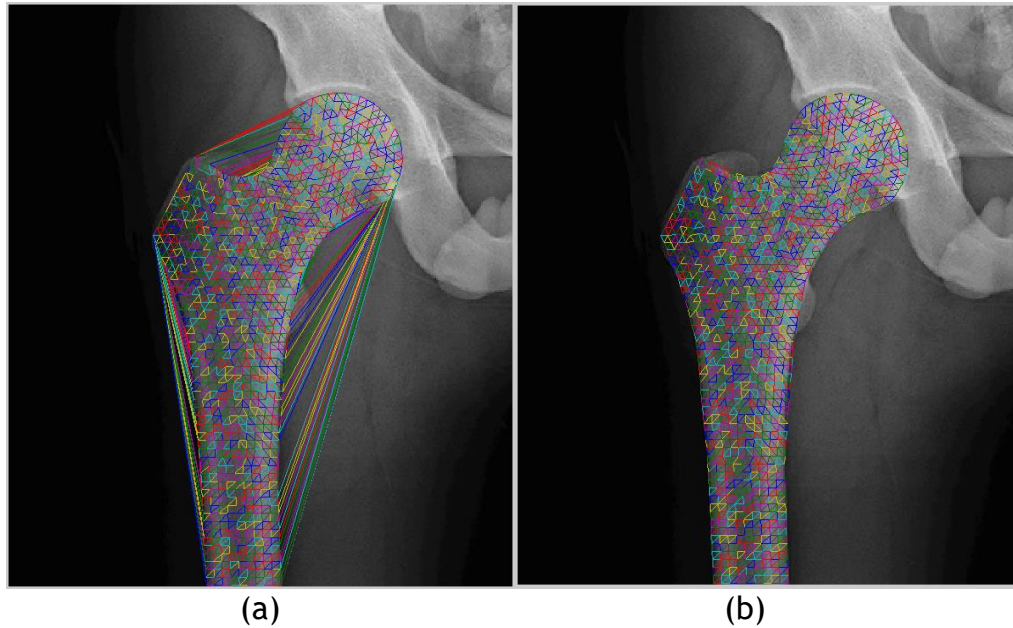
Figure 7.11 – Elements generated using the delaunay function before applying the verification methods – (a) – and after applying the verification methods – (b)

7.3.8 – From coordinates to dimensions

After having defined the elements and the nodal mesh, one last step is required before performing the finite element analysis. This step is the conversion of image coordinates to physical dimensions. To do this, a relation found in Polishchuk et al's work [92] was enforced.

In an article from 2013, Polishchuk et al. aims to predict the femoral head size given the patient's age, height, gender and race, following equation (7.29).

$$FHS(mm) = 10.5 + 3 \cdot G + 0.53 \cdot H + 0.0015 \cdot A - 1 \cdot R \tag{7.29}$$

In this equation, FHS stands for the femoral head size which is measured, in turn, through its diameter and this measurement is predicted in millimetres. G represents the gender and it takes the value of 1 for men and 0 for women. H is the height of the patient in inches. A expresses the patient's age in years and lastly, R describes the patient's race taking the value of 0 for Caucasian and 1 for others. Using this equation, the authors obtained an intra-class correlation coefficient (ICC) of 0.9 between predicted and implanted femoral head size.

The relevance and impact of the last parameter of race was somewhat questionable since no other information was found on the impact of race in determining the femoral head size, and it would also only impact a maximum of 1 mm. Therefore, in the algorithm developed this factor is not taken into consideration leaving the resultant expression to compute the femoral head size as demonstrated in equation (7.30).

$$FHS(mm) = 10.5 + 3 \cdot G + 0.53 \cdot H + 0.0015 \cdot A \tag{7.30}$$

With this relationship established, a simple linear correlation can determine the dimensions of the entirety of the nodes.

7.3.9 - Determination of the stiffness matrix

To implement the finite element method the algorithm was based on the formulation described in chapter 5.

To compute each element's stiffness matrix, the definition of its $\boldsymbol{B}$ matrix, $\boldsymbol{D}$ matrix and the volume of the element – dV – is required as described in equation 5.9. Starting with the determination of the $\boldsymbol{B}$ matrix, the derivatives of the shape functions for each node need to be established, equation (5.11). Since the algorithm works solely with triangular elements, there is no need to resort to the natural coordinate system.

The shape function determines the impact of each node in the deformation or stress inside the element, when applied to solid mechanics. An example of its application can be found in equation (7.31), where $\boldsymbol{u}(x_I)$ stands for the element's displacement, $\boldsymbol{N}(x_I)$ the element's shape functions and $\boldsymbol{u}$ the nodal displacements.

$$\boldsymbol{u}(x_I) = \boldsymbol{N}(x_I) \cdot \boldsymbol{u} \tag{7.31}$$

The element's nodal displacements can also be defined through equation (7.32). $\boldsymbol{p}(x_I)$ defines a vector with the elements coordinates, represented in equation (7.33) and $\boldsymbol{a}$ the vector with coefficients correlating the element's position with its displacement. It is important to highlight that the algorithm works with 2D finite element analysis. Therefore this demonstration will be exploring that same condition.

$$\boldsymbol{u}(x_I) = \boldsymbol{p}(x_I)^T \cdot \boldsymbol{a} \tag{7.32}$$

$$\boldsymbol{p}(x_I) = \begin{bmatrix} 1 & x_I & y_I \end{bmatrix} \tag{7.33}$$

When equation (7.32) is applied to the three nodes forming the element, equation (7.34) arises in which the $\boldsymbol{C}$ matrix represents the coordinates for the nodes as represented in equation (7.35).

$$\boldsymbol{u} = \boldsymbol{C} \cdot \boldsymbol{a} \;\;\Rightarrow\;\; \boldsymbol{a} = [\boldsymbol{C}]^{-1} \cdot \boldsymbol{u} \tag{7.34}$$

$$\boldsymbol{C} = \begin{bmatrix} 1 & x_1 & y_1 \\ 1 & x_2 & y_2 \\ 1 & x_3 & y_3 \end{bmatrix} \tag{7.35}$$

Replacing the $\boldsymbol{a}$ vector in equation (7.32), equation (7.36) is the result, and comparing it with equation (7.31), the equality found in equation (7.37) can be established.

$$\boldsymbol{u}(x_I) = \boldsymbol{p}(x_I)^T \cdot [\boldsymbol{C}]^{-1} \cdot \boldsymbol{u} \tag{7.36}$$

$$\boldsymbol{N}(x_I) = \boldsymbol{p}(x_I)^T \cdot [\boldsymbol{C}]^{-1} \tag{7.37}$$

As mentioned previously, since only triangular elements are being used, the $\boldsymbol{p}(x_I)^T$ vector is defined as seen in equation (7.33). Therefore, while computing the element's shape function derivatives all values are constant and do not depend on the point's position. Hence, simply resorting to the nodal coordinates, which are present in the $\boldsymbol{C}$ matrix, the derivative of the shape function is reached and with it, the $\boldsymbol{B}$ matrix is determined through equation (5.11).

To estimate the elasticity matrix, $\boldsymbol{D}$, two physical properties are required which are the elasticity modulus – E – and the Poisson coefficient - v. For the problem addressed with the algorithm, the plane strain deformation theory is considered, thus to compute the $\boldsymbol{D}$ matrix, the equation found in (5.10) is used. While the Poisson coefficient is constant throughout the bone [93], having a value of 0.33, the elasticity modulus depends on the apparent density of the bone. This was previously explored in chapter 2 and, using Belinha's [12] proposed law, the Young's modulus can be computed. To obtain the apparent density of bone for each region a linear correlation was created in which the maximum intensity possible - 1 - found inside the bone related to the highest apparent density value – 2.1 g/cm^3 – while the lowest pixel intensity -0- corresponded to the lowest apparent density value – 0.1 g/cm^3. It is worth pointing out that for this finite element analysis, a single integration point was used. Accordingly, the intensity evaluated for the centre of each element was calculated through an average of the element's centre and its neighbourhood, as described in equation (7.38), in which $intensity_n$ represents the calculated average and $i(x_n + i, y_n + j)$ represents the intensity of each neighbouring pixel.

$$intensity_n = \frac{\sum_{i=-1}^{1}\sum_{j=-1}^{1} i(x_n + i, y_n + j)}{9} \tag{7.38}$$

Due to the nature of radiographs and the computational model two main problems arose. If the femoral border is placed outside the bone, it considers that region as low density bone, since the background has a lower intensity than the bone. Also, for the femoral head, the acetabulum is also contributing to the increase of intensity of those pixels. Regarding the first problem mentioned, the points that were part of the border of the model were identified and for each point the difference between the point's computed density and the closest point of

the model that was not part of the border was calculated. If that difference was larger than 0.2 g/cm^3 in absolute value, the border point would have the apparent density of the point inside the model. With respect to the femoral head, two cumulative steps were considered in an attempt to solve this problem. Firstly, the average of the intensity of the femoral head points was calculated as was the average intensity of the femoral neck points. The difference between these averages was computed, as demonstrated in equation (7.39). The resulting difference was subtracted to all the points of the femoral head in order to obtain results closer to the reality, shown in equation (7.40), where $g(x, y)$ represents the previous pixel intensity from the femoral head points and $h(x, y)$ represents the new pixel intensity for femoral head points.

$$diff = avg_{head} - avg_{neck} \qquad (7.39)$$

$$h(x, y) = g(x, y) - diff \qquad (7.40)$$

While this attenuates the difference between the neck and the head there is still an obvious drop between densities found in the interface of the femoral head and femoral neck, as seen in figure 7.12.
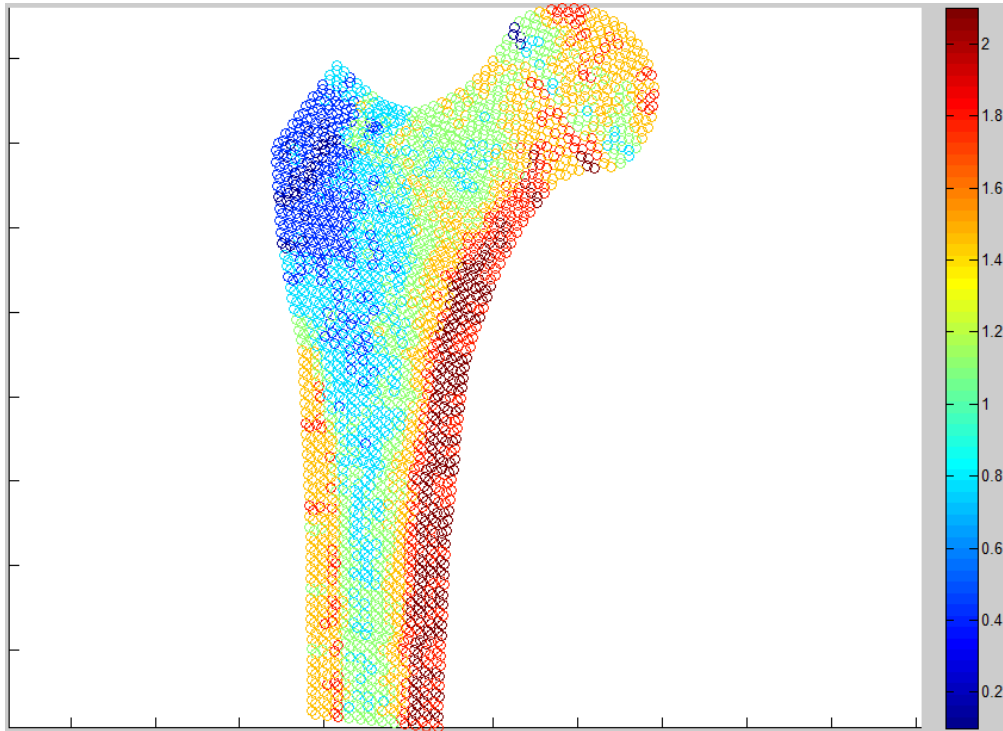
Figure 7.12 – Representation of obtained apparent densities on the femoral model with a coloured axis.

To mitigate this issue, another method is applied. This method evaluates the distance of each femoral head point to the neck and calculates the differences of intensities between each femoral head point and the closest femoral neck point, represented in equation (7.41). Multiplying by a factor which depends on the distance between the two points, displayed in equation (7.42), each head point has the calculated difference subtracted to its intensity value

– equation (7.43). With this, the computation of the femoral head points' intensities is finished and the apparent density can be calculated with ease.

$$diff = h(x, y) - n(x, y) \qquad (7.41)$$

$$factor = -\frac{1}{r} \cdot d + 1 \qquad (7.42)$$

$$i(x, y) = h(x, y) - diff \cdot factor \qquad (7.43)$$

In equation (7.41), $h(x, y)$ represents the intensity of each femoral head point and $n(x, y)$ the intensity of the closest neck point. For equation (7.42), r is the radius for the femoral head and d stands for the distance between the femoral head point and the neck point. Lastly, for equation (7.43), $i(x, y)$ reproduces the new femoral head point intensity.

The accumulation of both methods described creates a smooth and viable computation of apparent densities as is shown in figure 7.13
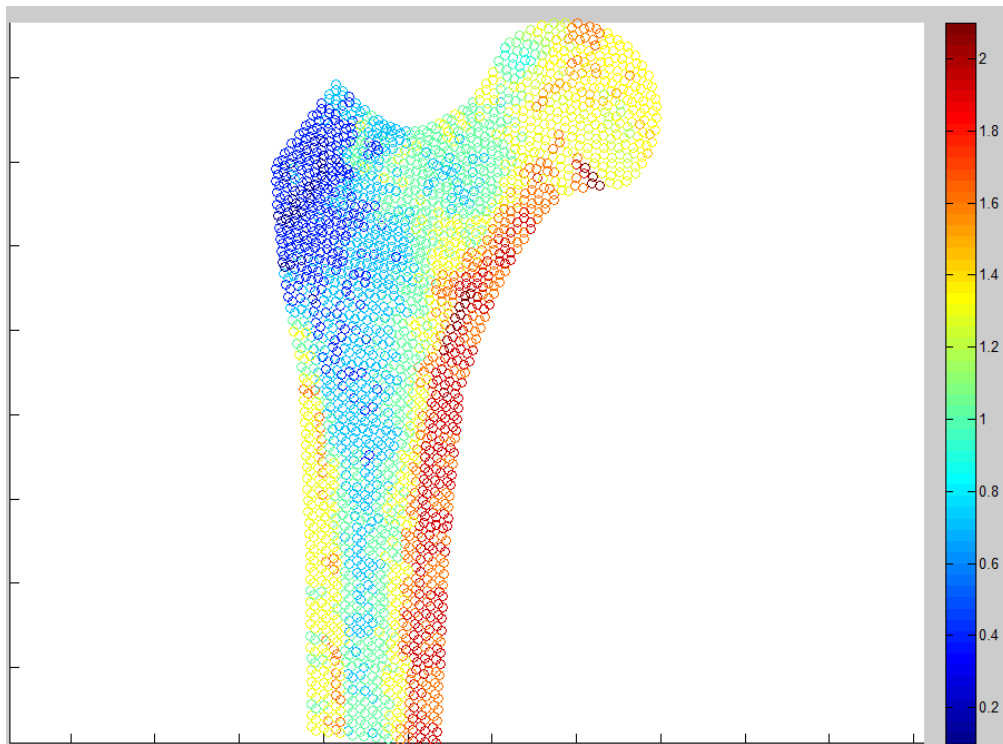
Figure 7.13 – Representation of obtained apparent densities on the femoral model with a coloured axis after applying both correction methods

Having calculated the apparent densities, the elasticity modulus can be determined with the equation (2.6) established by Belinha's proposed law. From then on, the **D** is calculated using equation (5.10).

To finally determine the element's stiffness matrix, the volume for each element is computed. Since, the mesh is composed of triangular elements, the element's volume can be calculated using equation (7.44). In this equation, V acts as the element's volume, A expresses

the area of the triangle that defines the triangular element and t depicts the thickness of the element.

$$V = A \cdot t \tag{7.44}$$

While the area of each element differs from each element, the thickness is a standard 1 mm. This thickness is determined by the average shaft diameter. The area on the other hand is set by half the norm of the cross product of two vectors that define the triangle, as represented in equation (7.45).

$$A = \frac{1}{2} \left\| v_{12} \times v_{13} \right\| \tag{7.45}$$

In this equation, v_{12} serves as the vector between points 1 and 2 in a triangle, while v_{13} portrays the vector between points 1 and 3.

Finally, the element's stiffness matrix can be computed through equation 5.9, and after all the elementary stiffness matrices are computed they are assembled in a global matrix as mentioned in chapter 5 with the example shown in equation (5.20).

7.3.10 - Forces applied and essential boundary conditions

Following the computation of the global stiffness matrix, the applied forces and the essential boundaries are applied.

Regarding the applied forces, there are two different forces which are taken into consideration. The mechanical case considered, as worked on by Belinha et al. [94], has a downward force applied in the femoral head with approximately twice the weight of the patient with an angle of 24° and an upward force applied in the greater trochanter with an angle of 28°, having a magnitude of 30% of the force applied in the femoral head. This mechanical case is represented in figure 7.14 and mimics the situation of a patient standing on one leg where the force applied into the femoral head is caused by the body weight, while the applied into the greater trochanter is caused by the abductor muscles [94].
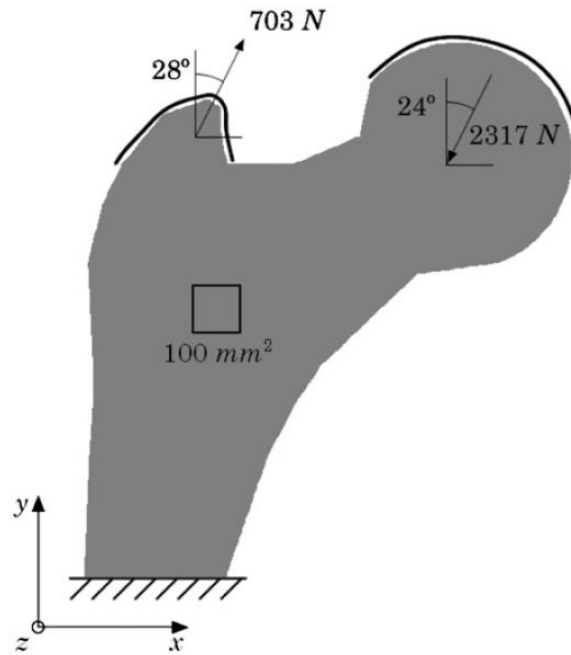
Figure 7.14 [94] – Mechanical situation considered for the analysis

In the situation presented in Belinha's work [94], nothing is said regarding the correlation between the weight of the patient and the magnitude of the forces applied, because his work followed the suggestion proposed by Beaupré et al. [95] and Rybicki et al. [96]. In discussion, it was ascertained that the magnitude of the forces presented in figure 7.13 were a result of a patient weighing 100Kg.

Notice that the femur is not supporting the body's full weight, but simply the weight of the structures above it. To calculate this distribution, the values proposed by Törzeren [97] are used, which are represented in table 7.1, that distribute the body's full weight into its components by a percentage.

Body part	Percentage
Torso	50.8%
Head	7.3%
Arm	2.7%
Forearm	1.6%
Hand	0.66%

Table 7.1 [97] – Body weight distribution into its upper components

Totalling a percentage of approximately 68%, the femur supports the weight of around two-thirds of our body, and this weight will be applied to the femoral head in the mechanical situation previously seen.

Both forces are applied throughout a surface in bone, as is evident in the representation in figure 7.13. That distribution was considered as a parabolic one, in which the integral should add up to the total force applied, as represented in figure 7.15.
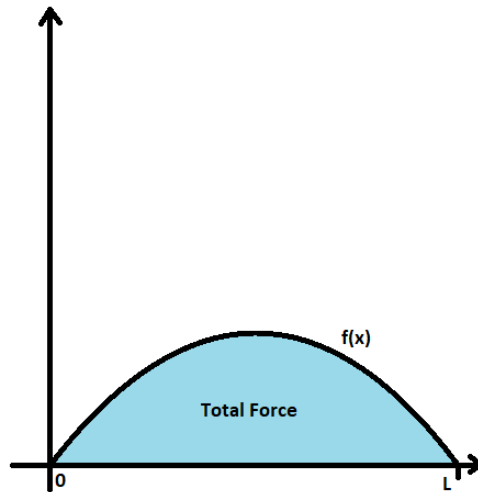
Figure 7.15 – Representation of the function of distribution of forces throughout a surface

This method was applied for the developed algorithm in which the result can be seen in figure 7.16.
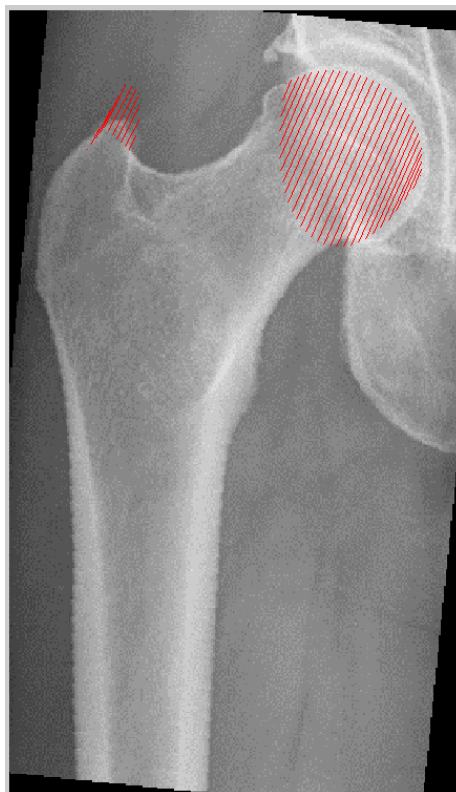
Figure 7.16 – Representation of the distribution of forces applied in the femoral model

As performed before, it is paramount that the femur is presenting itself in an upright position so as to have the angles properly calculating the distribution of forces in the x and y axis. The magnitude of the forces is projected into the x and y axis of the picture, and a force

vector, $\boldsymbol{F}$, is created. This vector contains the force of all nodes in the x and y direction, having a dimension of $2n \times 1$, being n the number of nodes existent in the model. For the nodes, in which the aforementioned forces are applied, the projection of the value is placed while in others that value is 0.

After the creation of the force vector, the essential boundary is defined. For analysed cases, the essential boundary defined is the fixation of the bottom of the shaft. In this fixation, no movement is allowed either in the horizontal or the vertical direction. To enforce this fixation the penalty method is applied as mentioned in chapter 5. That penalization occurs for the nodes that constitute the bottom of the shaft as represented in figure 7.17

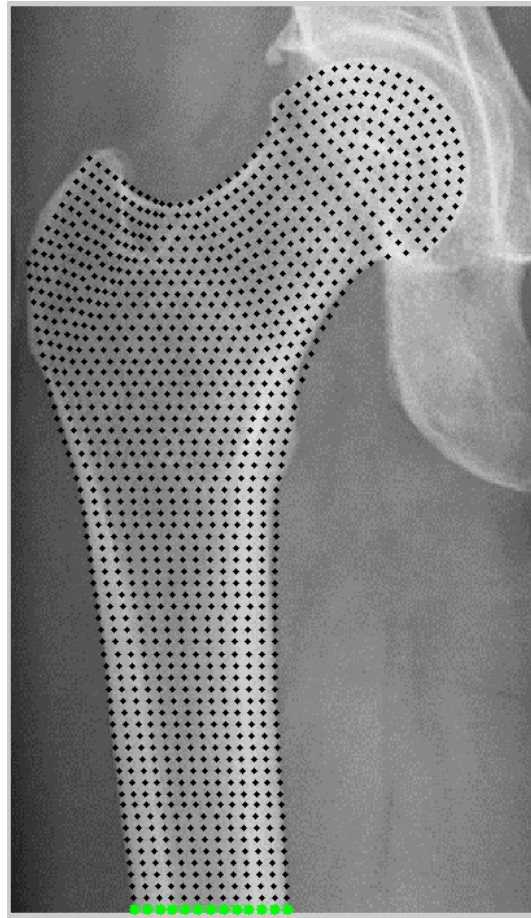**Figure 7.17** – Representation of elements nodes (black points) with the fixated nodes highlighted (green points)

Since, the nodes which the essential boundary is applied do not have forces applied on them, no penalty is enforced in those nodes in the force vector.

With the penalised stiffness matrix, and the force vector defined, the displacement vector for each node can be calculated using equation (5.22).

7.3.11 - Stress and strain calculation

As seen in chapter 5 with equations (5.24) and (5.25), the stress and strain tensors for each element can be calculated using the element's elasticity matrix, D, and displacement differentiation matrix, B. This is the following step performed by the algorithm, however these are not the displayed properties.

From the stress tensor, which takes the form displayed in equation (7.46), the software computes the effective, or von Mises, stress.

$$\sigma = \begin{bmatrix} \sigma_{xx} & \tau_{xy} & \tau_{xy} \\ \tau_{xy} & \sigma_{yy} & \tau_{yz} \\ \tau_{xz} & \tau_{yz} & \sigma_{zz} \end{bmatrix} \tag{7.46}$$

To compute the von Mises stress, the principal stresses are computed through the eigenvalues of the stress tensor. This generates two values, since the considered case is a plane stress problem. To calculate the von Mises stress from these eigenvalues, the equation (7.47) is used.

$$\sigma_{vm} = \sqrt{(\sigma_1 - \sigma_2)^2 + (\sigma_2 - \sigma_3)^2 + (\sigma_3 - \sigma_1)^2} \tag{7.47}$$

In this equation, σ_1, σ_2 and σ_3 represent the calculated eigenvalues while σ_{vm} refers to the generated von Mises stress.

Besides the von Mises stress, the ratio between it and the ultimate compression stress is also calculated through equation (7.48), where σ^c acts as the ultimate compression stress.

$$ratio = \frac{\sigma_{vm}}{\sigma^c} \tag{7.48}$$

The ultimate compression stress however is not yet known, and its calculation is defined by Belinha's proposed law [12] where the value for the ultimate compression stress relies on the apparent density of bone in the considered element. The equation demonstrating the computation of the apparent density can be found in equation 2.7. This ratio serves as a measure of endangerment of fracture risk of bone. If the ratio is above 1, this means the effective stress felt on the element is higher than its ultimate stress, which is an indicator for potential bone fracture/damage.

7.4 - Software Interface

The developed software presents an interface that allows the user to navigate through the software and contains several valuable characteristics. In this subchapter, some screenshots of the software's interface are displayed, and the functions available to the user are thoroughly detailed.
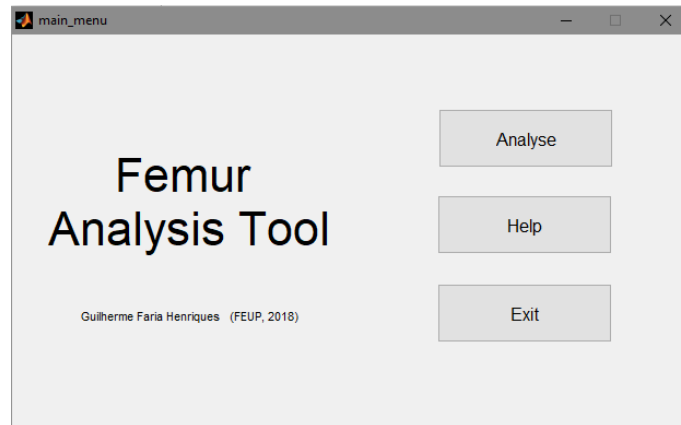
Figure 7.18 – Main menu interface

The main menu interface presents three buttons. The "Help" button generates a pop-up window with the authors email for any questions regarding the software. "Exit" terminates the program and, lastly, "Analyse" proceeds to the analysis of a femoral radiograph. By pressing the "Analyse" button, a pop-up window opens allowing for the user to select a femoral radiograph to be analysed.

After this, another window arises, in which the user inputs the patient's information, namely its age, weight in Kg, height in cm and gender – figure 7.19. Additionally, this interface presents the selected image in the side.

Figure 7.19 – Patient information interface

Following the input of the patient's information, a window is launched for the radiograph to be cropped, if necessary.
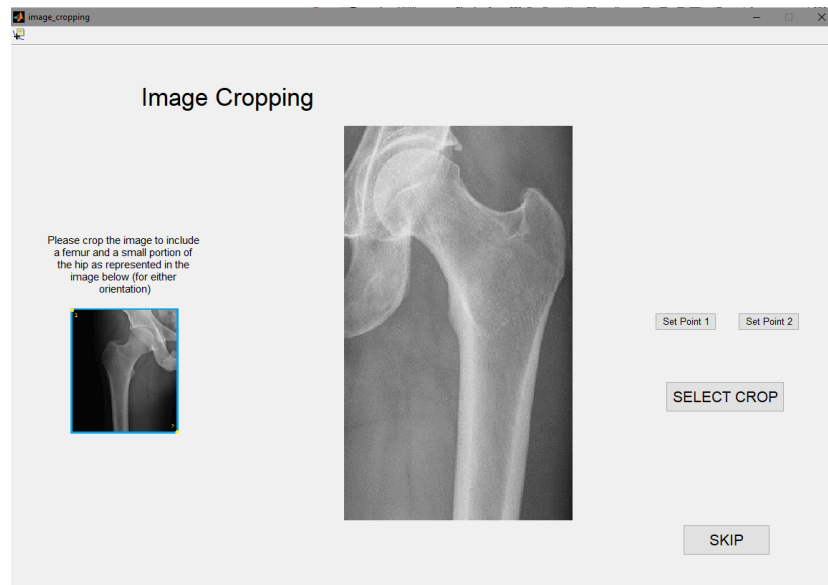
Figure 7.20 – Image cropping interface

With this tool, the software can read double femoral radiographs – as frequently happens in hip X-rays – and crop the image at this stage. In the left-hand side an example on how the cropping should be performed is presented. In the case that the crop is not necessary, the user can simply hit the "Skip" button.

After the orientation detection is performed, the result might be unclear, if it falls on those that do not meet the requirements mentioned previously. If that occurs, an interface window lets the user manually select the orientation of the femur – figure 7.21.
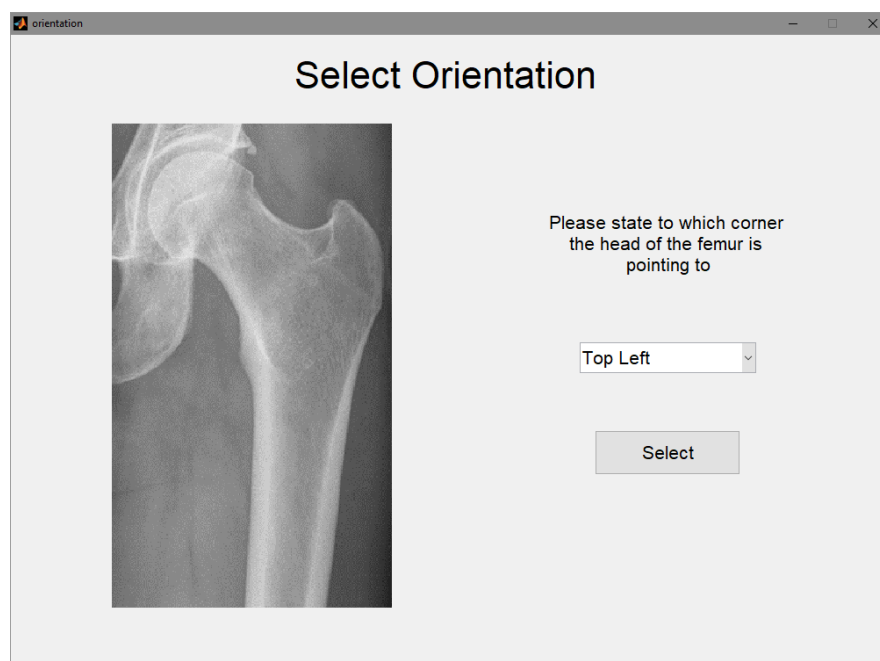
Figure 7.21 – Orientation selection interface

From then, the background algorithm computes de gradients and the interface window regarding the thresholding step appears, as shown in figure 7.22.
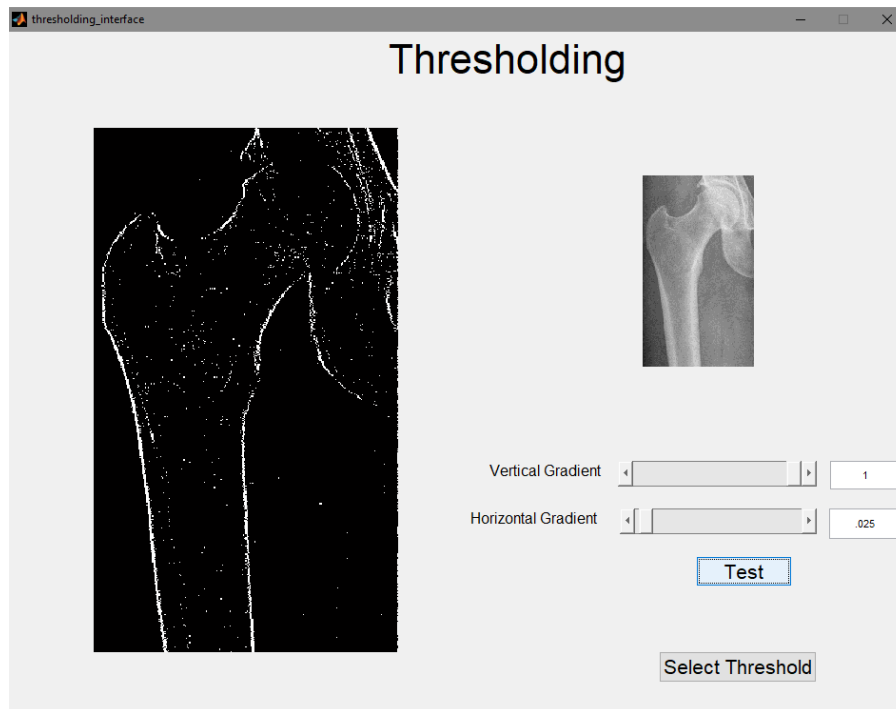
Figure 7.22 – Thresholding interface

This interface allows the user to select the appropriate threshold to generate the border-defining binary images for both the horizontal gradient and the vertical gradient. The two limits can be set by the user either resorting to the slider bar which ranges from 0 to 1, or using the writable text boxes to the side. The "Test" button applies the thresholds to the gradients and displays the image seen on the left of figure 7.22, which is a union of the binary image from the horizontal threshold and the vertical threshold.

When the user is satisfied with the image portrayed, the "Select Threshold" button is pushed and the model retrieval algorithm ensues.

The subsequent interface shows a possible model for the femur, as is represented in figure 7.23.
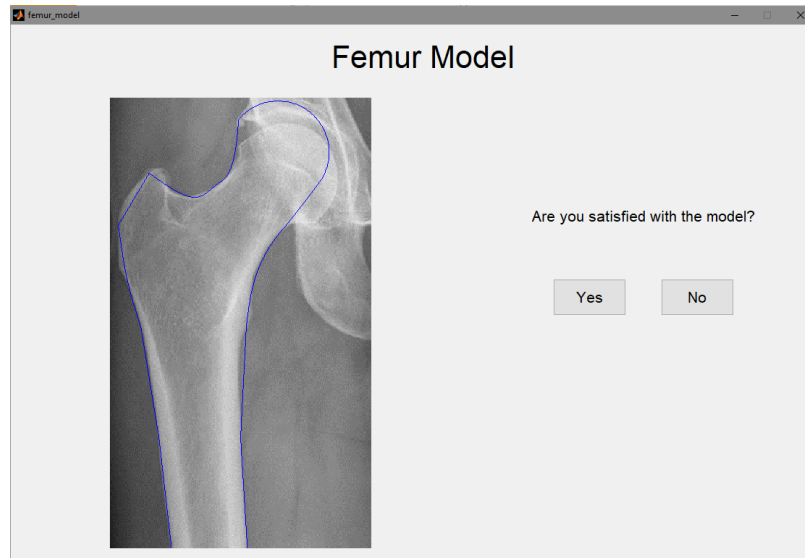
Figure 7.23 – Femur model interface

The interface allows the user to either proceed with the analysis or correct the model suggested. In figure 7.23, we see some problems with the femoral head. Thus, by pressing the "No" button, an interface permitting the model correction emerges, represented in figure 7.24.
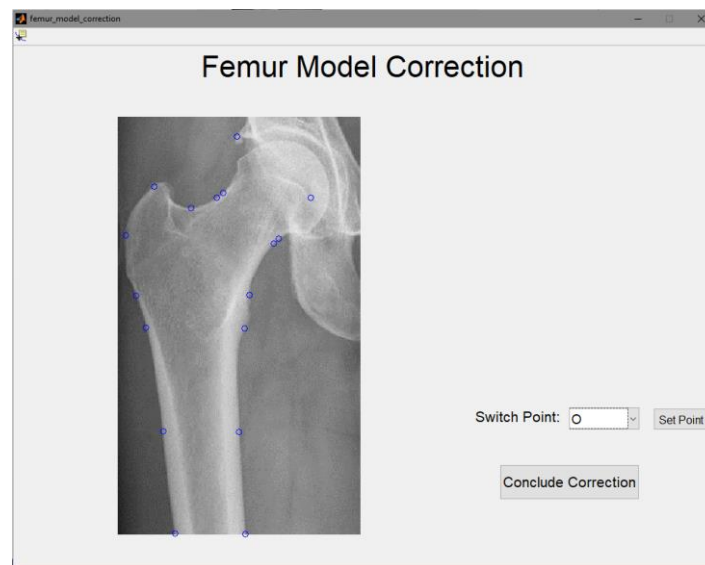
Figure 7.24 – Femur model correction interface

This interface presents the user with the reference points in which the femoral model is based on. The arrangement of these points should follow the ones described in figure 7.7. To change any point, the user uses the point selection tool in the top left corner to select the correct position, and making use of the dropdown list, selects the point he wishes to change. The "Set Point" button confirms the change and displays the point's new position. After all corrections are performed the button "Conclude Correction" is pressed and the window confirming the femoral model opens again with the recent femur model. The femoral model should look like the one demonstrated in figure 7.25.
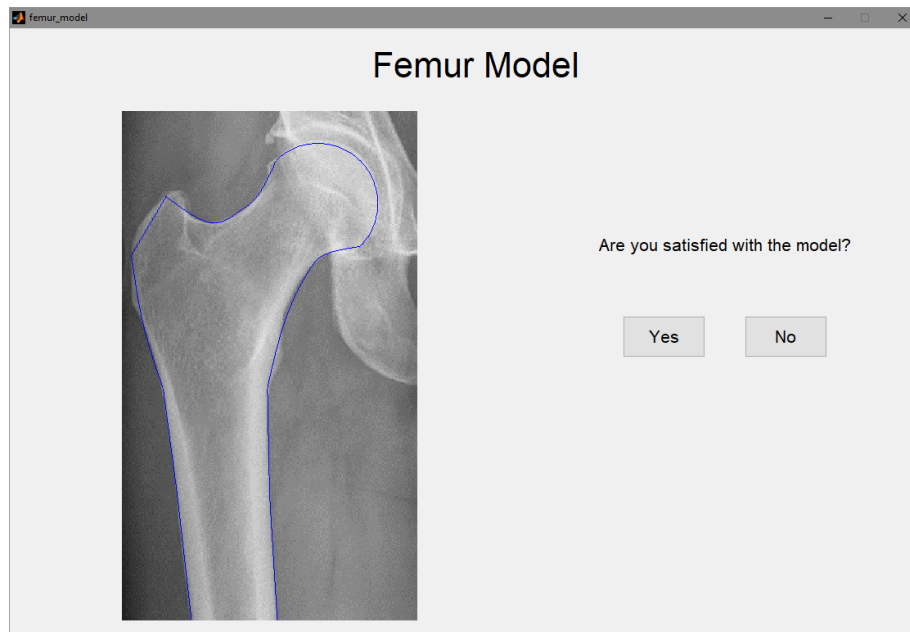
Figure 7.25 – Femur model presented after corrections

Having selected the "Yes" button in the interface, the algorithm performs the mechanical analysis on the resulting model. As soon as the calculations are executed, the results interface is displayed, as it is seen in figure 7.26.
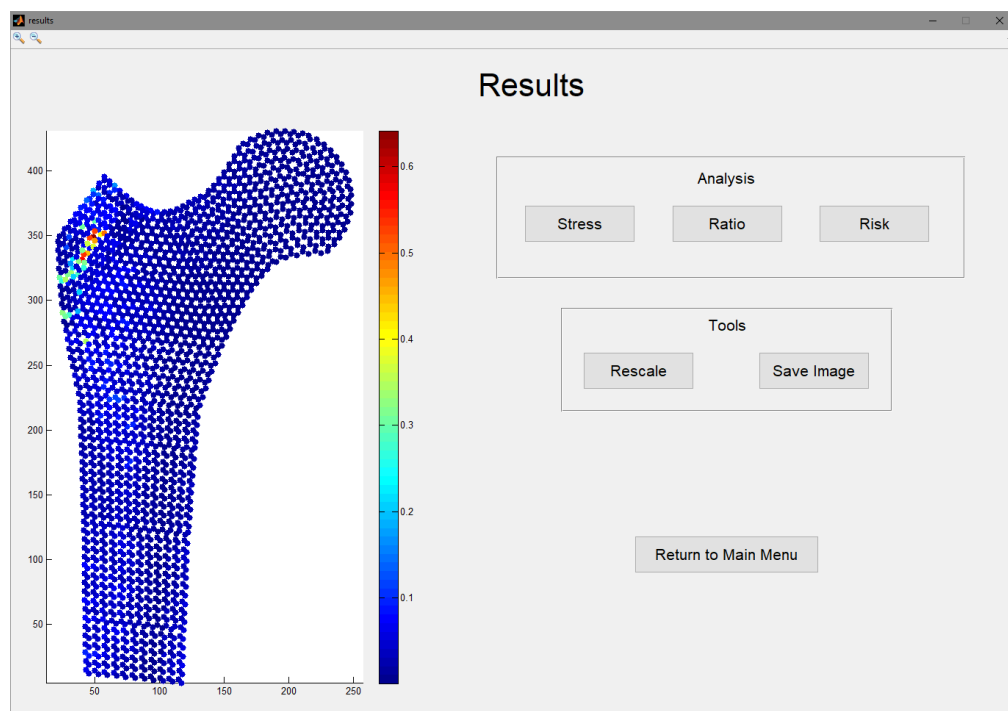
Figure 7.26 – Results interface displaying the calculated ratio

By default, this interface first presents the ratio between the effective stress and the ultimate stress, however, by interacting with the analysis buttons, the user can see the von Mises stress, by pressing the button "Stress", the aforementioned ratio, and the risk which

simply highlights points with a ratio higher than 1. In figure 7.27, the interface displays the von Mises stress distribution throughout the model.
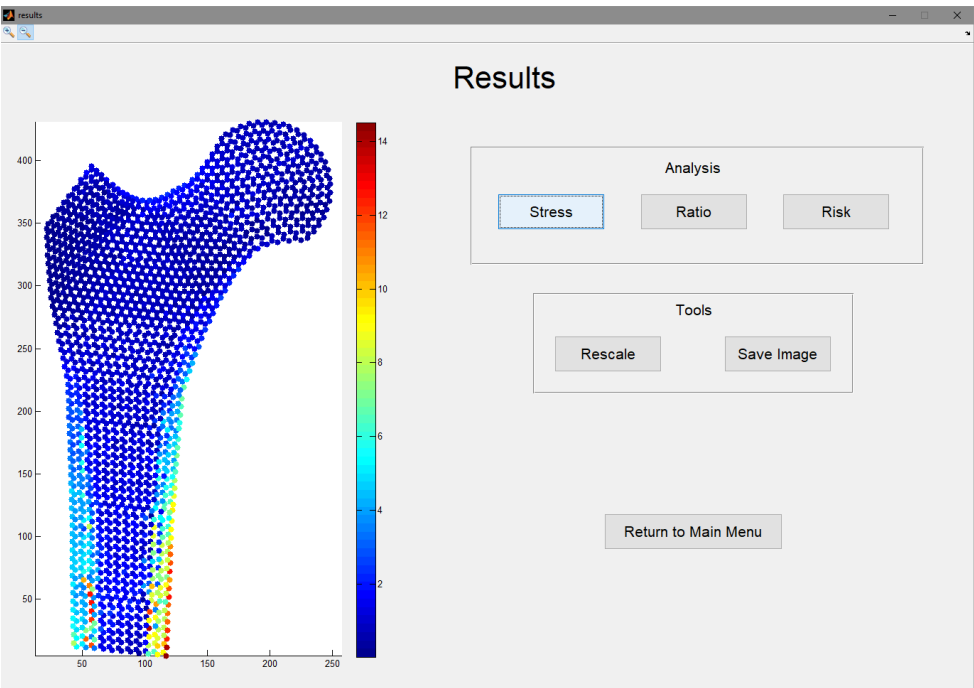
Figure 7.27 – Results interface displaying the von Mises stress

Two important tools worth mentioning are the "Rescale" and "Save Image" buttons. The first one, applies a rescale to the image if the zoom tool is used. This is particularly helpful if the user intends to investigate specific areas such as the femoral neck and wants to see with better detail the distribution of the chosen property. In figure 7.28, the result is presented.
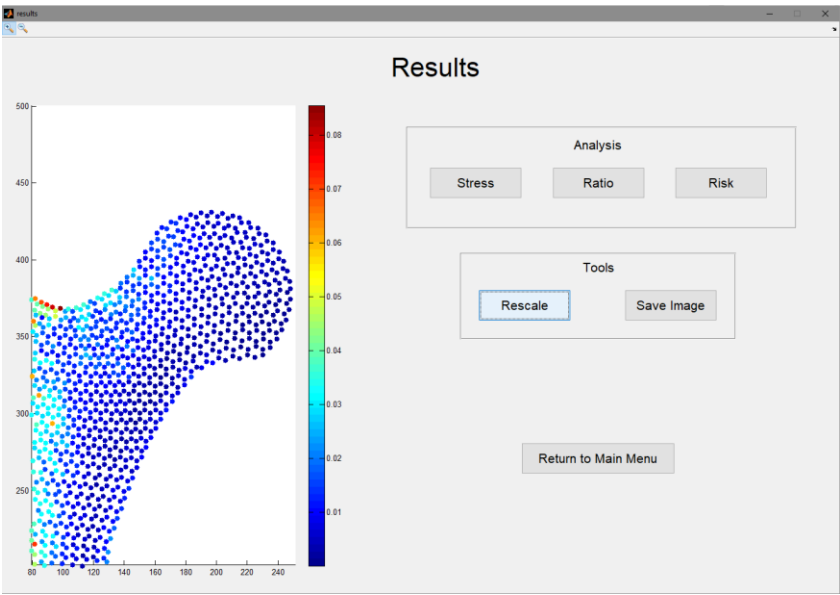
Figure 7.28 – Results interface displaying the ratio with a new scale appropriate for the exhibited window

The "Save Image" button saves the image displayed on the axis into an image file on a chosen directory for the user.

Lastly, the "Return to Main Menu" button sends the user to the main menu interface where the process can restart.

Chapter 8

Results and discussion

8.1 - Results

In this section, the results are presented for the following five cases:

- 50 year-old male patient, weighing 75Kg, with 175cm
- 50 year-old male patient, weighing 120Kg, with 175cm
- 50 year-old male patient, weighing 75Kg, with 175cm (with a different radiograph)
- 50 year-old male patient, weighing 75Kg, with 175cm diagnosed with a chondrosarcoma
- 50 year-old male patient, weighing 75Kg, with 175cm diagnosed with an osteosarcoma

The results are displayed in their image form accompanied with the original scan. These results are presented with the original radiograph and the computed apparent density distribution, effective stress and ratio between the effective stress and the ultimate compression stress. With these outcomes, the aim is to assess the effect of weight with the same conditions, and also evaluate the software's response to different radiographs.

The discussion of the results is present in the following subchapter.

Figure 8.1 – Apparent density, von Mises stress and ratio distribution (from top right to bottom right) with original radiograph (left) from 50 year-old male patient, weighing 75Kg, with 175cm
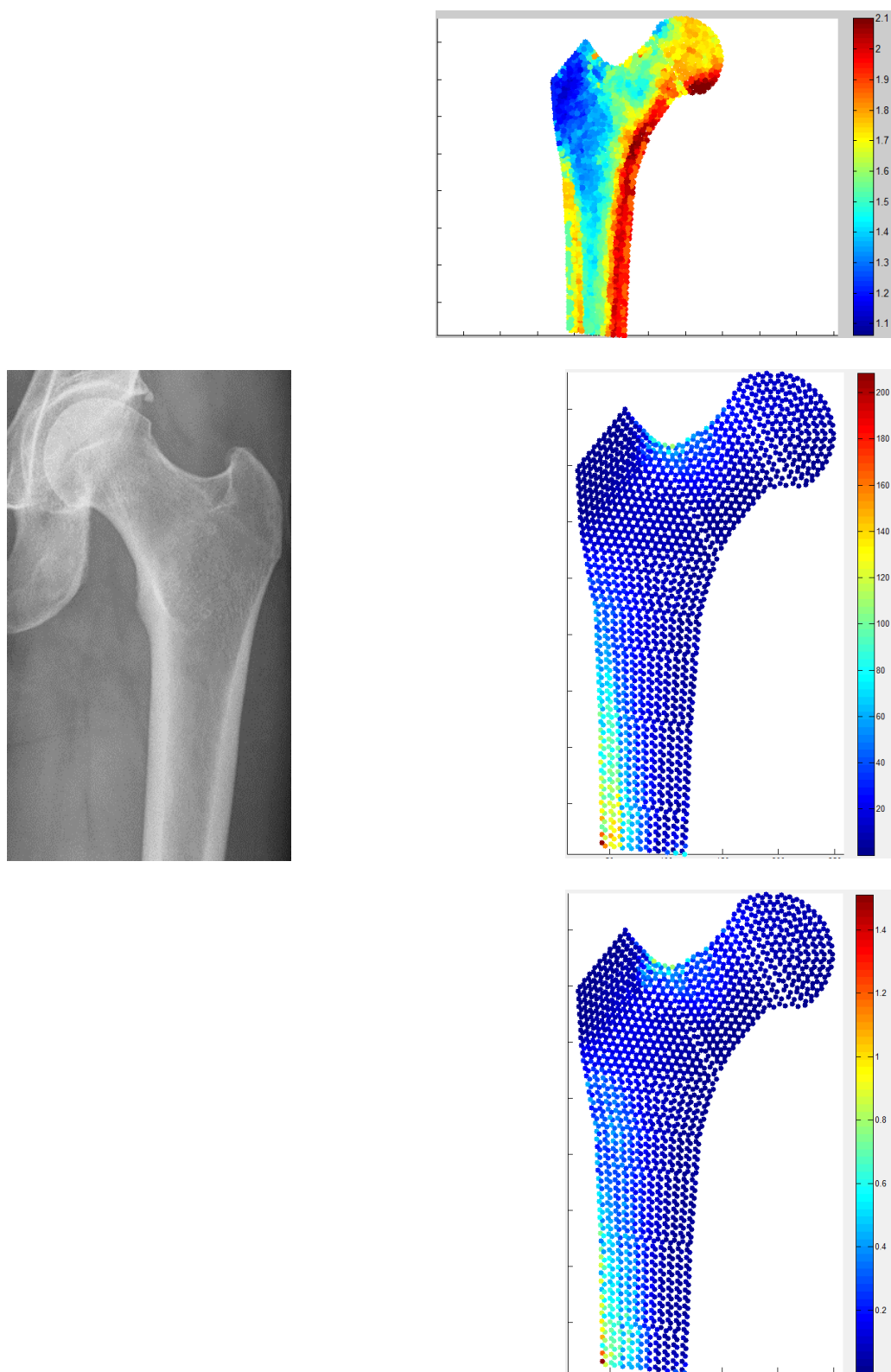
Figure 8.2 – Apparent density, von Mises stress and ratio distribution (from top right to bottom right) with original radiograph (left) from 50 year-old male patient, weighing 120Kg, with 175cm
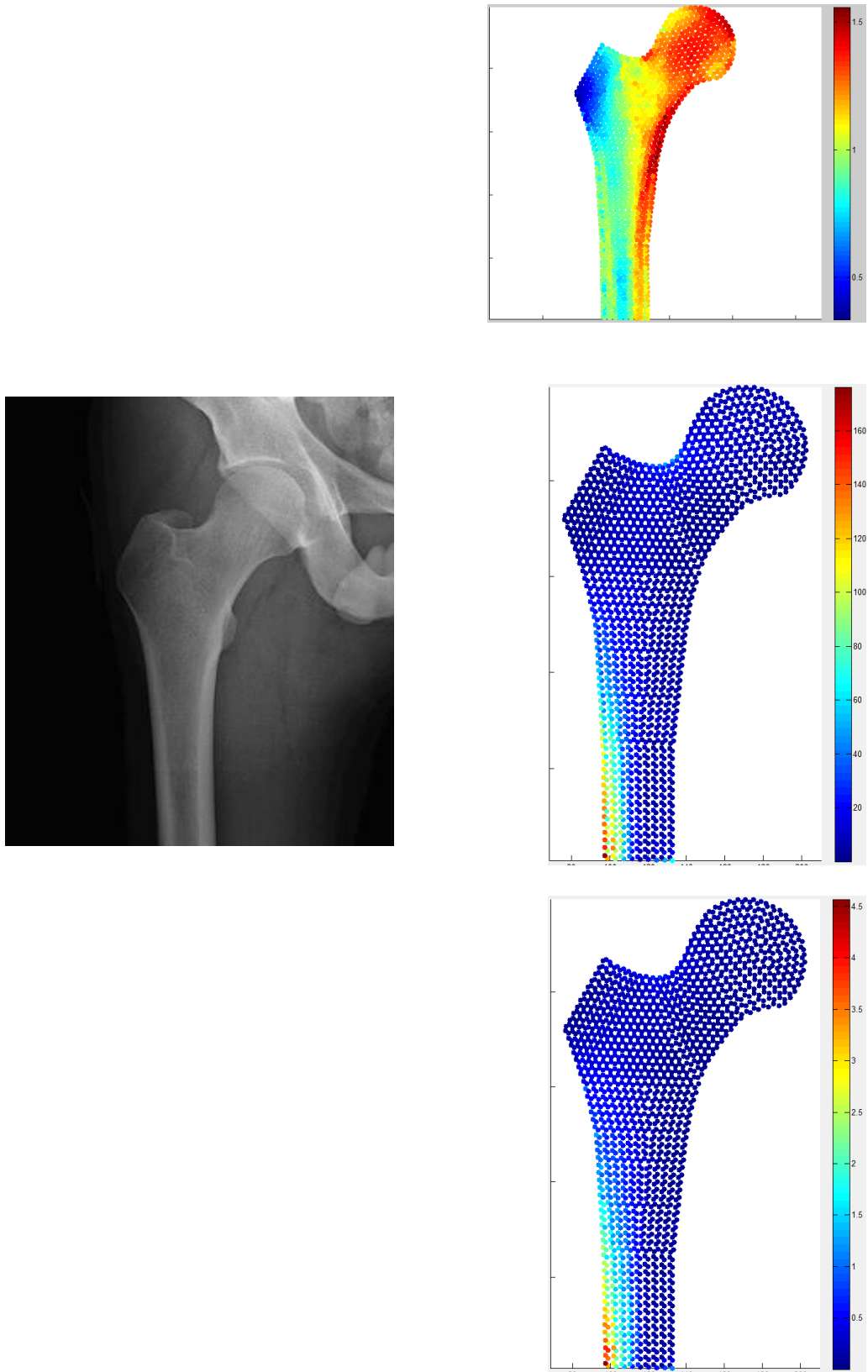
Figure 8.3 – Apparent density, von Mises stress and ratio distribution (from top right to bottom right) with original radiograph (left) from 50 year-old male patient, weighing 75Kg, with 175cm

Figure 8.4 – Apparent density, von Mises stress and ratio distribution (from top right to bottom right) with original radiograph (left) from 50 year-old male patient, weighing 75Kg, with 175cm diagnosed with a chondrosarcoma

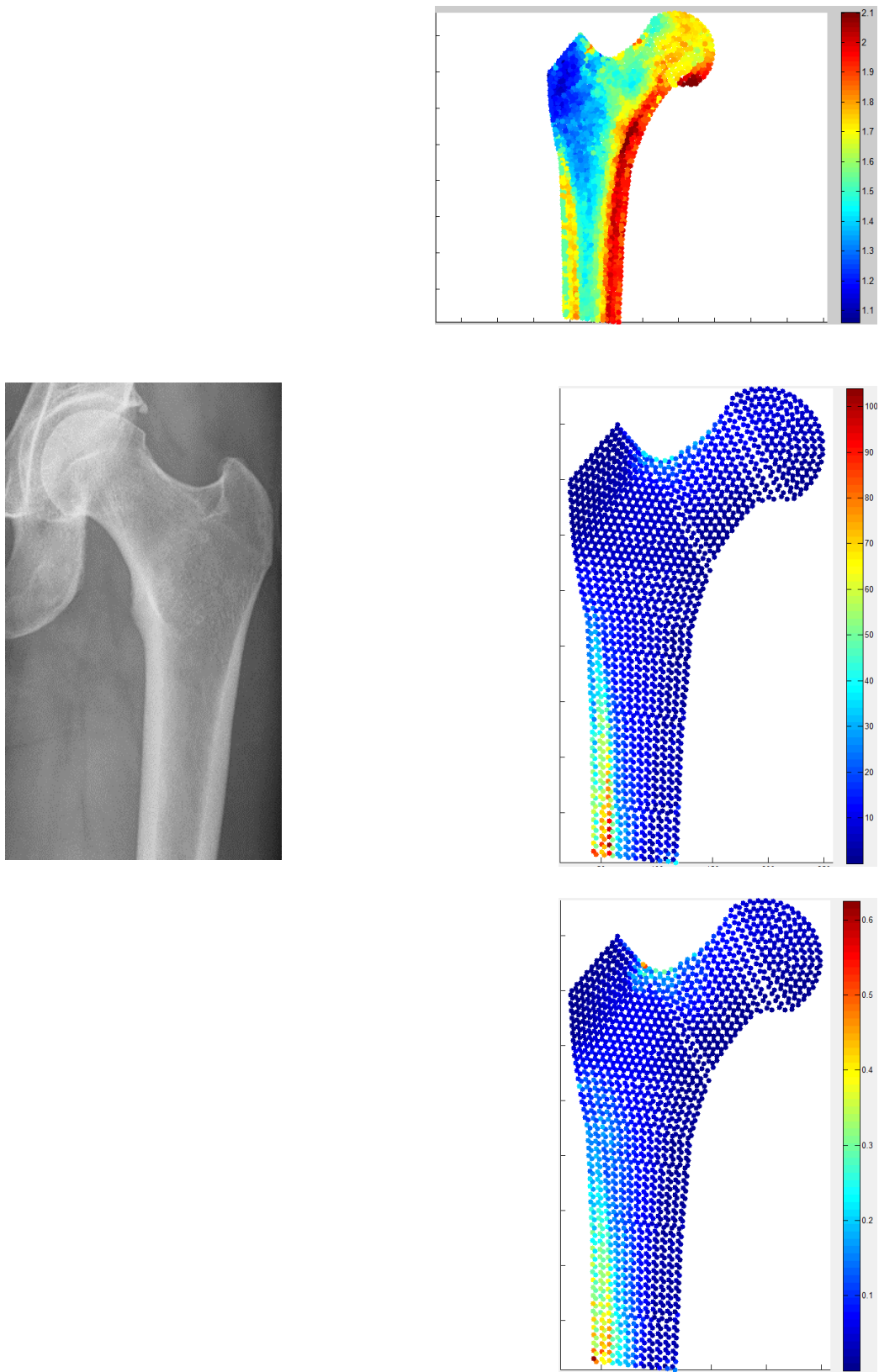**Figure 8.5** – Apparent density, von Mises stress, ratio and risk distribution (from top right to bottom right) with original radiograph (left) from 50 year-old male patient, weighing 75Kg, with 175cm diagnosed with an osteosarcoma
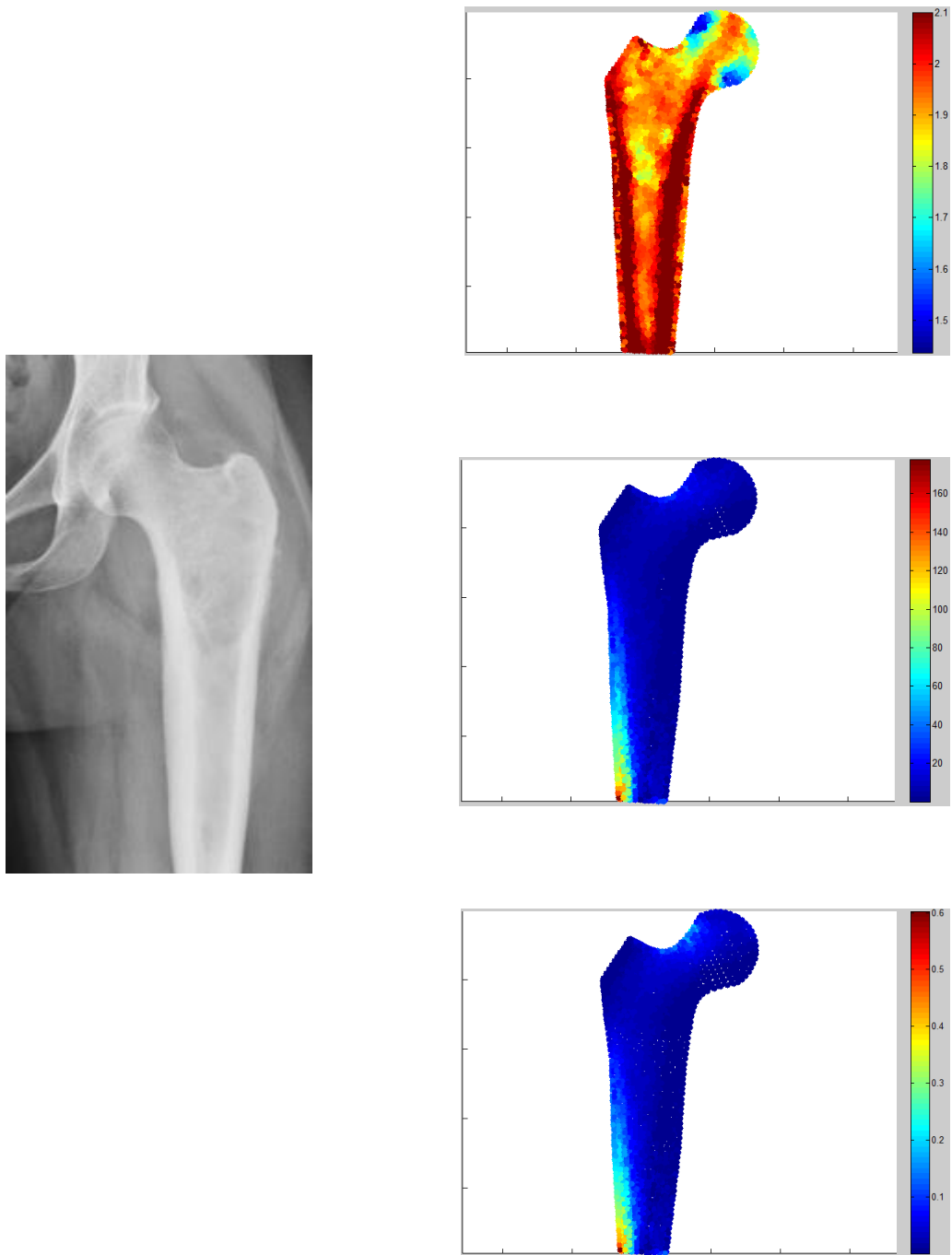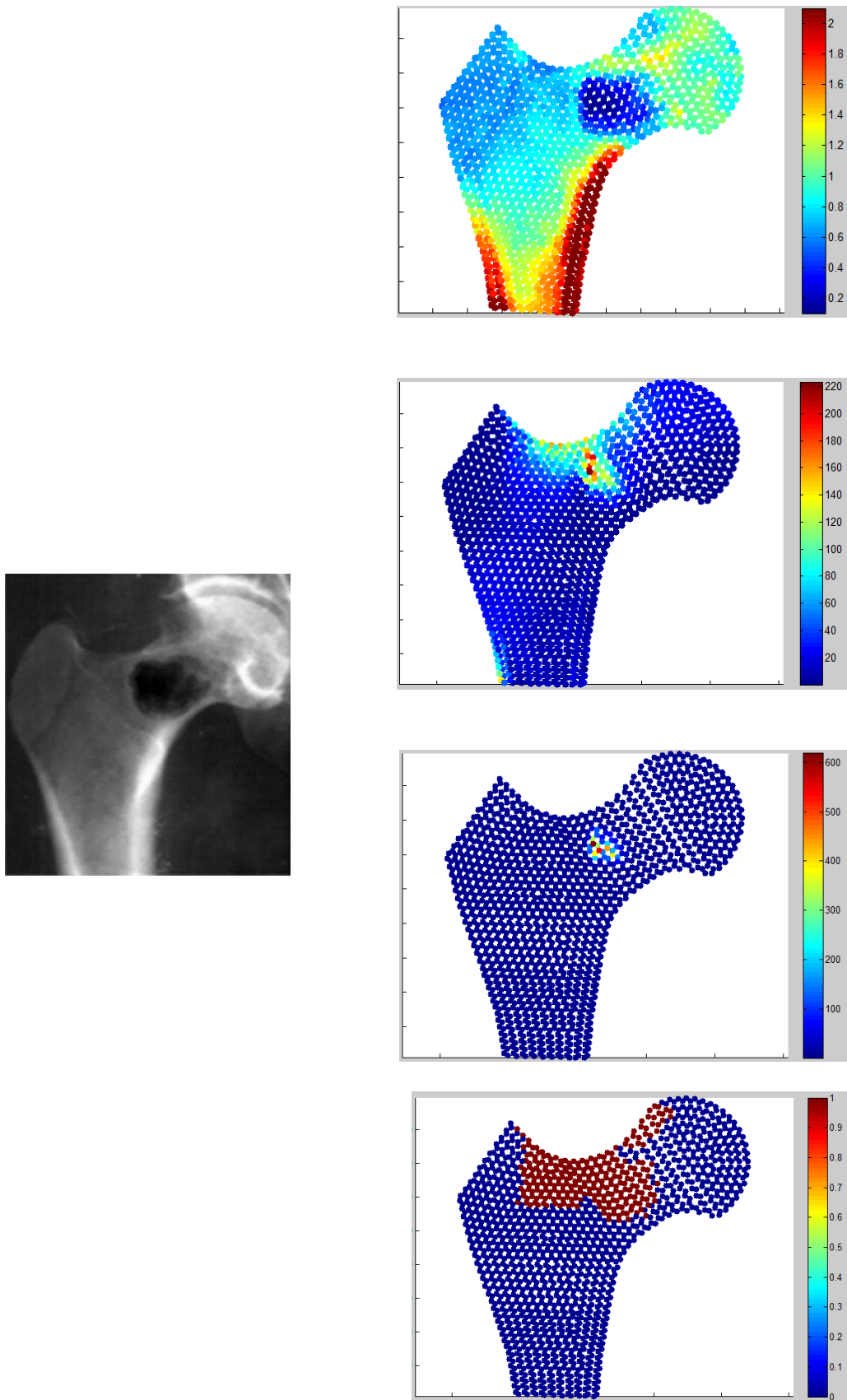
8.2 - Discussion

From the set of images presented, the results are displayed as images as well. This was chosen due to the nature of the software being the qualitative evaluation of the outcomes and not a quantitative evaluation. In figure 8.1, the algorithm showed a good performance in the determination of the model. It did have some problems with the determination of the femoral head, as seen in a previous chapter, demonstrated in figure 7.23. However with the adjusted corrections, the resulting model allows a FEA, which produces good results as shown in figure 8.1. The apparent density obtained is congruent with the real values. The highest values are presented in the cortical layer of bone while the trabecular bone shows a decrease in apparent density. This is seen in the middle portion of the shaft, in the greater trochanter and femoral neck. Between the medial and lateral side of cortical bone there is some difference shown in apparent density which is due to the nature of the radiographs. In these, the lateral portion of bone is usually darker in comparison to the medial portion. When analysing the stress applied in the elements, the values match up to the expected values, with the cortical lateral portion of the shaft saturating most of the stress in the bone (with a slight value raise in the upper neck area). When analysing the ratio between von Mises stress and ultimate stress, this is mostly observed in the lateral shaft region. Due to the nature of the stress distribution, this area obtains the higher values. Nonetheless, these values are low and not pose a risk of fracture at all.

Between figures 8.1 and 8.2, the only difference was the weight of the patient. Since the model is the same, and the apparent densities are too, the pattern of the stress distribution is the similar. However the values are increased, since the forces applied are also increased. In the first figure, the stress values go up to near 100 MPa and the ratio up to 0.65. However, in the second figure, the effective stress jumps to close to 210 MPa and the ratio up to 1.4. The ratio values seen in figure 8.2, show an increased fracture risk. However, the points with values above 1 are minor and are very close to the lateral border. This could be explained by the fact that the lateral border of the femoral shaft picks up lower intensity regions and, hence, displays a lower apparent density region.

In figure 8.3 another radiograph is tested with the metrics for the patient of 50 years old, 175 cm and 75 Kg. Regarding the model generation, the algorithm is capable of detecting the femur's shape. However, the finite element analysis reaches contradictory results with the expected outcome. While the von Mises stress distribution looks coherent, the apparent density and ratio tell a different story. Due to the improper apparent density obtained throughout the model, where the femoral head with trabecular bone shows a greater density than cortical bone in the left side of the shaft, the calculated ratios are inconsistent with reality, showing the region with largest ratio on the cortical portion of the shaft. When the ultimate stresses are analysed, figure 8.6, it is possible to observe that where the cortical lateral portion of the shaft should have a higher ultimate stress it is still showing decreased values.
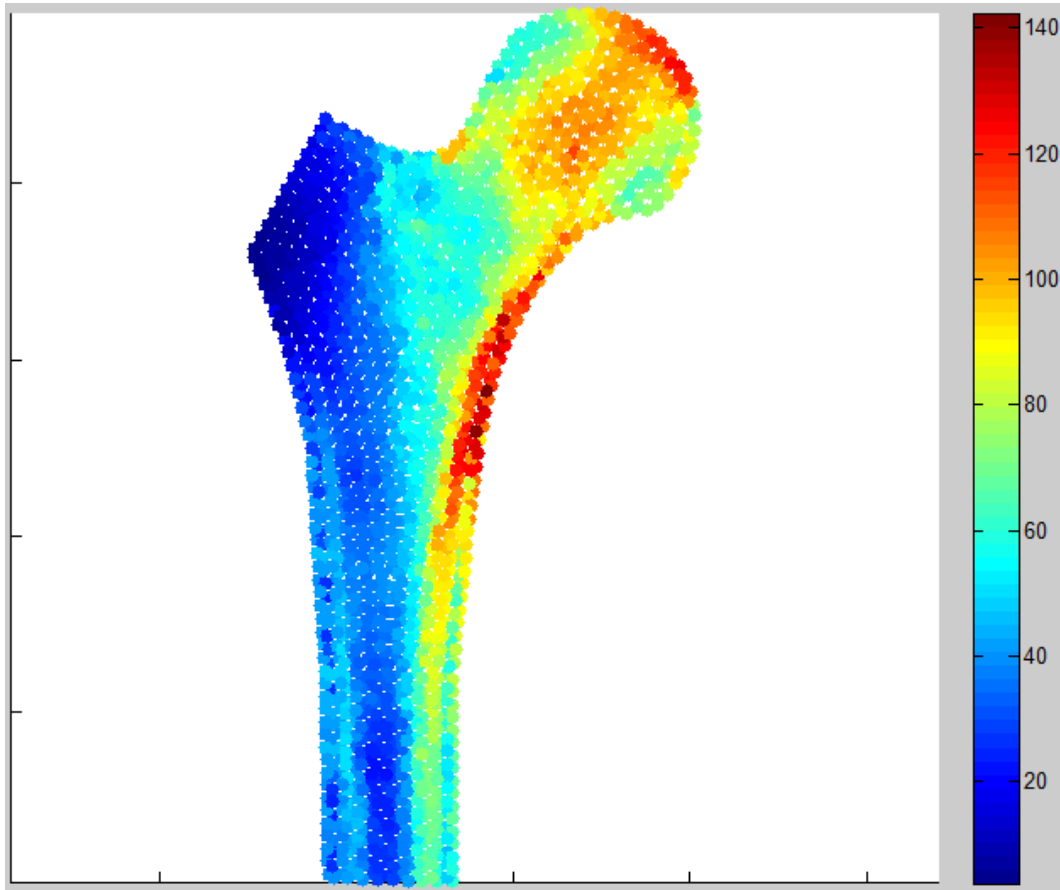
Figure 8.6 – Ultimate stress distribution for the radiograph obtained in figure 8.3

The darkening of the lateral region heavily affects this model and in the bottom region this effect is even more obvious. Adding to this the transition between cortical bone and trabecular bone is not as evident as in other radiographs. The developed algorithm is not capable to efficiently distinguishing cortical and trabecular bone if their intensity values are close. Therefore, the algorithm performance increases with better contrast between these two regions.

For the last two radiographs, the algorithm was not able to assert a femoral model. In radiograph of figure 8.4, the presence of high intensity transitions in the background did not allow the algorithm to detect the model. Regarding the radiograph of figure 8.5, the blurriness of the radiograph made it impossible to get a good detection with the gradient calculation. For these scans, the reference points were manually inserted and the model was developed from those points. The algorithm was able to execute all the remaining steps.

In figure 8.4, the radiograph displays a femur with a chondrosarcoma. Despite the presented mass near the lesser trochanter region the algorithm is not able to detect said mass. In the apparent density distribution, a decrease is seen around that region but only a slight one. The biggest decreases occur in the femoral head. Upon discussion with some physicians, it was found that the regions marked with a low apparent density are merely artefacts produced by the radiograph itself. Since the overall image has a bright intensity, the values for apparent density are presented with high values across the model. In fact, with the model having the lowest value of apparent density at around 1.45, the entire bone is considered as cortical bone.

Clearly, this is a problem and the need for higher contrast between trabecular and cortical regions is reinforced.

Lastly, regarding figure 8.5, a radiograph is presented with a massive osteosarcoma in the femoral neck region. This osteosarcoma is fairly well detected by the algorithm, as visible from the apparent density distribution presented. And it becomes even more visible when observing the ratio distribution on the computational model. When the radiographs show a heavy loss of bone mass due to a tumour, the algorithm can detect the tumours presence as is displayed in figure 8.5. This is further supported when figure 8.7 is observed, displaying all the regions from the radiograph presented in figure 8.5, with a ratio superior to 1, meaning there is a risk of fracture.
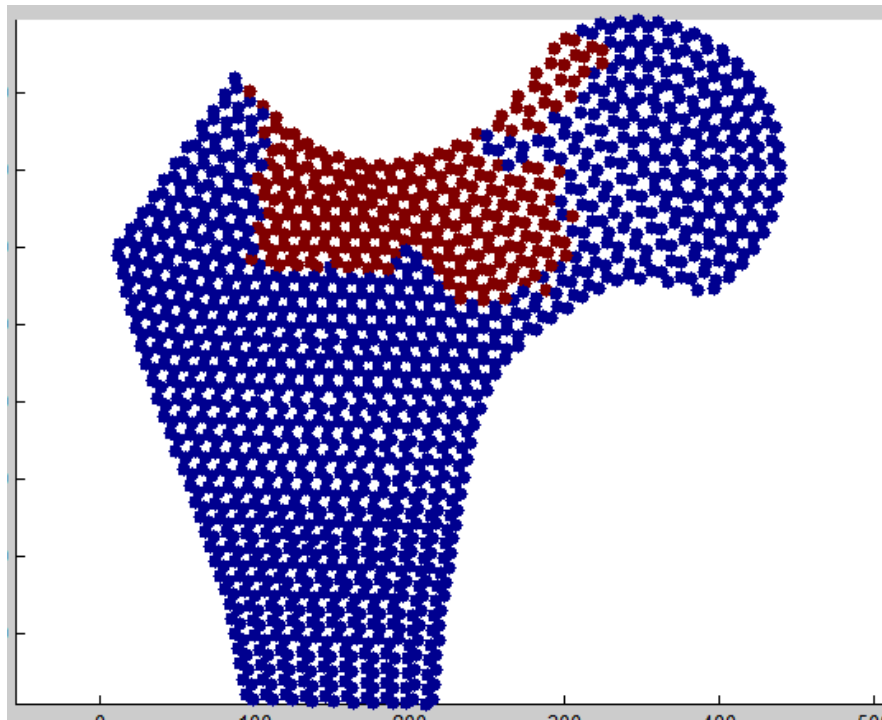
Figure 8.7 – Representation of elements with a ratio superior to 1 presented in dark red and under 1 presented in blue

Analysing all the results attained, it is possible to arrive at some conclusion regarding the developed software. If the radiograph shows pronounced contrast between bone and the background, the algorithm is able to achieve a possible femoral model. Though it may have some slight errors with the model, they are easily adjustable using the software's interface. Also, a meaningful contrast between cortical and trabecular regions is key to reach plausible results. This should also be something to consider by the user when utilizing this tool.

Chapter 9

Conclusions and Future Work

The presented software is still far from being a final product. However, it is a considerable stepping stone for the development of a future application to be used in a clinical environment. Femur Analysis Tool has some hallmarks that makes it stand out, such as the automatic detection of the femur and its interactivity with the physician allowing it to take control of the femoral model at any time. The possibilities of such application reaching the clinical environment are promising, especially with a well-developed product, since it brings information to the physician which is not available to him at the moment in the form of X-ray analysis, providing great benefit to the world of orthopaedics.

The developed application showed promising results with well-defined radiographs and it was capable to detect prevalent osteosarcomas. However, with this study some major lessons were learned regarding the capabilities of the software. To provide an automatic femoral model, the original radiograph should provide clear distinction between bone and background, not display high gradient values in the background and have clear image definition. Adding to that, to provide adequate stress analysis, the key aspect to consider is having a good contrast between trabecular and cortical bone.

This field can continue its stride to achieve a software able to provide the clinicians with the tools they need. To create this product some further steps can be taken to increase the quality in femoral model generation and stress analysis. As an example, more complex technique can be applied to either pre-process the image or detect the femoral border in the X-ray. This can also be achieved using self-learning methods, such as machine learning, in which the algorithm adapts as it analyses data. Regarding the stress analysis, some work can be performed in levelling the brightness throughout the scan in order to reach correct apparent densities.

Furthermore, other implementations that can be carried out is the addition of hip prosthesis models and performing a stress evaluation of the femoral bone with the prosthetic.

References

[1] H. Maradit Kremers *et al.*, "Prevalence of Total Hip and Knee Replacement in the United States.," *J. Bone Joint Surg. Am.*, vol. 97, no. 17, pp. 1386–97, Sep. 2015.

[2] Canadian Institute for Health Information, "Hip and Knee Replacements in Canada: Canadian Joint Replacement Registry 2015 Annual Report," 2015.

[3] S. Kurtz, K. Ong, E. Lau, F. Mowat, and M. Halpern, "Projections of Primary and Revision Hip and Knee Arthroplasty in the United States from 2005 to 2030," *J. Bone Jt. Surg.*, vol. 89, no. 4, p. 780, Apr. 2007.

[4] I. S. Vanhegan, A. K. Malik, P. Jayakumar, S. U. Islam, and F. S. Haddad, "A financial analysis of revision hip arthroplasty - THE ECONOMIC BURDEN IN RELATION TO THE NATIONAL TARIFF," *J Bone Jt. Surg Br*, vol. 94-B, no. 5, pp. 619–23, 2012.

[5] American Academy of Orthopaedic Surgeons, "MANAGEMENT OF HIP FRACTURES IN THE ELDERLY EVIDENCE-BASED CLINICAL PRACTICE GUIDELINE," 2014.

[6] S. Dixon, "Diagnostic Imaging Dataset Statistical Release", 2016.

[7] S. Standring, *Gray's Anatomy The Anatomical Basis of Clinical Practice*, 40th ed. Elsevier, 2008.

[8] A. L. Kierszenbaum and L. Tres, *Histology and Cell Biology: An Introduction to Pathology.*, 3rd ed. W B Saunders Co, 2012.

[9] A. C. Hall and J. E. Guyton, *Textbook of medical physiology*, 11th ed. Philadelphia: WB Saunders, 2005.

[10] D. L. Longo, A. S. Fauci, D. L. Kasper, S. L. Hauser, J. L. Jameson, and J. Loscalzo, Eds., *Harrison's Principles of Internal Medicine*, 18th ed. New York, Chicago, San Francisco, Lisbon, London, Madrid, Mexico City, Milan, New Delhi, San Juan, Seoul, Singapore, Sydney, Toronto: McGraw Hill Medical, 2012.

[11] BruceBlaus, "Osteoporosis Locations." [Online]. Available: https://upload.wikimedia.org/wikipedia/commons/thumb/a/af/Osteoporosis_Locations.png/1024px-Osteoporosis_Locations.png.

[12] J. Belinha, *Meshless Methods in Biomechanics, Bone Tissue Remodelling Analysis*. Porto: Springer, 2014.

[13] J. C. Lotz, T. N. Gerhart, and W. C. Hayes, "Mechanical properties of metaphyseal bone in the proximal femur.," *J. Biomech.*, vol. 24, no. 5, pp. 317–29, 1991.

[14]   P. Zioupos, R. B. Cook, and J. R. Hutchinson, "Some basic relationships between density values in cancellous and cortical bone," *J. Biomech.*, vol. 41, no. 9, pp. 1961–1968, Jan. 2008.

[15]   US Food and Drug Administration, "Medical Imaging," 2018. [Online]. Available: https://www.fda.gov/Radiation-EmittingProducts/RadiationEmittingProductsandProcedures/MedicalImaging/default.htm. [Accessed: 03-Jun-2018].

[16]   C. A. Roobottom, G. Mitchell, and G. Morgan-Hughes, "Radiation-reduction strategies in cardiac computed tomographic angiography.," *Clin. Radiol.*, vol. 65, no. 11, pp. 859–67, Nov. 2010.

[17]   J. H. Scatliff and P. J. Morris, "From Roentgen to magnetic resonance imaging: the history of medical imaging.," *N. C. Med. J.*, vol. 75, no. 2, pp. 111–3.

[18]   P. C. Lauterbur, "Image Formation by Induced Local Interactions: Examples Employing Nuclear Magnetic Resonance," *Nature*, vol. 242, no. 5394, pp. 190–191, Mar. 1973.

[19]   Herman Yaggi Carr, "Free precession techniques in nuclear magnetic resonance," Harvard University, 1953.

[20]   J. Radon, "Uber die Bestimmung von Funktionen durch ihre Integralwerte Langs Gewisser Mannigfaltigkeiten," *Ber. Saechsische Akad. Wiss*, vol. 29, p. 262, 1917.

[21]   W. H. Oldendorf, "The quest for an image of brain: a brief historical and technical review of brain imaging techniques.," *Neurology*, vol. 28, no. 6, pp. 517–33, Jun. 1978.

[22]   D. W. McRobbie, E. A. Moore, M. J. Graves, and M. R. Prince, *MRI: From picture to proton*, 2nd ed. Cambridge: Cambridge University Press, 2006.

[23]   S. Dixon, "Diagnostic Imaging Dataset Statistical Release Diagnostic Imaging Dataset Statistical Release," 2017.

[24]   University of Conneticut Health Centre, "Computerized Tomography chapter," 2016. [Online]. Available: http://fitsweb.uchc.edu/ctanatomy/extrem/index.html.

[25]   Lawrence M. Davis MD, "CT Scan (CAT Scan, Computerized Axial Tomography)," 2017. [Online]. Available: https://www.emedicinehealth.com/ct_scan/article_em.htm#when_to_seek_medical_care.

[26]   Eurostat, "Healthcare resource statistics - technical resources and medical technology," 2017.

[27]   P. Suetens, *Fundamentals of medical imaging*, 2nd ed. Cambridge University Press, 2009.

[28]   L. Vincent, P. Soille, and P. Soille, "Watersheds in digital spaces: an efficient algorithm based on immersion simulations," *IEEE Trans. Pattern Anal. Mach. Intell.*, vol. 13, no. 6, pp. 583–598, Jun. 1991.

[29] A. Yezzi, S. Kichenassamy, A. Kumar, P. Olver, and A. Tannenbaum, "A geometric snake model for segmentation of medical imagery," *IEEE Trans. Med. Imaging*, vol. 16, no. 2, pp. 199–209, Apr. 1997.

[30] J. A. Noble and D. Boukerroui, "Ultrasound image segmentation: a survey," *IEEE Trans. Med. Imaging*, vol. 25, no. 8, pp. 987–1010, Aug. 2006.

[31] V. Chalana and Y. Kim, "A methodology for evaluation of boundary detection algorithms on medical images," *IEEE Trans. Med. Imaging*, vol. 16, no. 5, pp. 642–652, 1997.

[32] S. C. Mitchell, J. G. Bosch, B. P. F. Lelieveldt, R. J. van der Geest, J. H. C. Reiber, and M. Sonka, "3-D active appearance models: segmentation of cardiac MR and ultrasound images," *IEEE Trans. Med. Imaging*, vol. 21, no. 9, pp. 1167–1178, Sep. 2002.

[33] N. Friedland and D. Adam, "Automatic ventricular cavity boundary detection from sequential ultrasound images using simulated annealing," *IEEE Trans. Med. Imaging*, vol. 8, no. 4, pp. 344–353, 1989.

[34] M. Mulet-Parada and J. A. Noble, "2D+T acoustic boundary detection in echocardiography," *Med. Image Anal.*, vol. 4, no. 1, pp. 21–30, Mar. 2000.

[35] A. T. Stavros, D. Thickman, C. L. Rapp, M. A. Dennis, S. H. Parker, and G. A. Sisney, "Solid breast nodules: use of sonography to distinguish between benign and malignant lesions.," *Radiology*, vol. 196, no. 1, pp. 123-134, Jul. 1995.

[36] K. Drukker, M. L. Giger, K. Horsch, M. A. Kupinski, C. J. Vyborny, and E. B. Mendelson, "Computerized lesion detection on breast ultrasound," *Med. Phys.*, vol. 29, no. 7, pp. 1438–1446, Jun. 2002.

[37] Y. Yan Kang, K. Engelke, and W. A. Kalender, "A new accurate and precise 3-D segmentation method for skeletal structures in volumetric CT data," *IEEE Trans. Med. Imaging*, vol. 22, no. 5, pp. 586–598, May 2003.

[38] P. K. Saha and F. W. Wehrli, "Measurement of Trabecular Bone Thickness in the Limited Resolution Regime of In Vivo MRI by Fuzzy Distance Transform," *IEEE Trans. Med. Imaging*, vol. 23, no. 1, pp. 53–62, Jan. 2004.

[39] M. R. Kaus, V. Pekar, C. Lorenz, R. Truyen, S. Lobregt, and J. Weese, "Automated 3-D PDM construction from segmented images using deformable models," *IEEE Trans. Med. Imaging*, vol. 22, no. 8, pp. 1005–1013, Aug. 2003.

[40] N. Baka *et al.*, "2D-3D shape reconstruction of the distal femur from stereo X-ray imaging using statistical shape models," *Med. Image Anal.*, vol. 15, no. 6, pp. 840–850, Dec. 2011.

[41] O. Bandyopadhyay, A. Biswas, and B. B. Bhattacharya, "Long-bone fracture detection in digital X-ray images based on digital-geometric techniques," *Comput. Methods Programs Biomed.*, vol. 123, pp. 2–14, Jan. 2016.

[42] Y. Chen, X. Ee, W. K. Leow, and T. Sen Howe, "Automatic Extraction of Femur Contours from Hip X-Ray Images," Springer, Berlin, Heidelberg, 2005, pp. 200-209.

[43]   R. Courant, "VARIATIONAL METHODS FOR THE SOLUTION OF PROBLEMS OF EQUILIBRIUM AND VIBRATIONS," *Bull. Amer. Math. Soc.*, vol. 49, pp. 1–23, 1943.

[44]   M. J. Turner, R. W. Clough, H. C. Martin, and L. J. Topp, "Stiffness and Deflection Analysis of Complex Structures," *J. Aeronaut. Sci.*, vol. 23, no. 9, pp. 805–823, Sep. 1956.

[45]   J. L. Synge, *The Hypercircle in Mathematical Physics: A Method for the Approximate Solution of Boundary Value Problems*. London: Cambridge Press, 1957.

[46]   J. H. Argyris, *Energy Theorems and Structural Analysis*, vol. 26, no. 10. MCB UP Ltd, 1954.

[47]   C. A. Felippa, *Introduction to Finite Element Methods*. Colorado: University of Colorado, 2004.

[48]   T. D. Brown, "Finite Element Modeling in Musculoskeletal Biomechanics," *J. Appl. Biomech.*, vol. 20, no. 4, pp. 336–366, Nov. 2004.

[49]   W. A. Brekelmans, H. W. Poort, and T. J. Slooff, "A new method to analyse the mechanical behaviour of skeletal parts.," *Acta Orthop. Scand.*, vol. 43, no. 5, pp. 301–17, 1972.

[50]   E. Hinton and D. R. J. Owen, *Finite Element Programming*. Swansea: Academic Press, 1977.

[51]   F. Castro and G. Henriques, "Fémur com Artroplastia Total da Anca: Uma Análise com o Método de Elementos Finits," Porto, 2016.

[52]   P. Lopes, "Atherosclerosis Biomechanical Simulation," Faculdade de Engenharia da Universidade do Porto, 2016.

[53]   COMSOL Multiphysics Cyclopedia, "Detailed Explanation of the Finite Element Method (FEM)." [Online]. Available: https://www.comsol.com/multiphysics/finite-element-method. [Accessed: 26-Jan-2018].

[54]   W. A. M Brekelmans *et al.*, "A NEW METHOD TO ANALYSE THE MECHANICAL BEHAVIOUR OF SKELETAL PARTS," *Acta orthop. Scandinav*, vol. 43, pp. 301–317, 1972.

[55]   R. Huiskes and E. Y. Chao, "A survey of finite element analysis in orthopedic biomechanics: the first decade.," *J. Biomech.*, vol. 16, no. 6, pp. 385–409, 1983.

[56]   R. Scholten, "Ueber die Berechnung der mechanischen Beanspruchung in Knochenstrukturen mittels fuer den Flugzeugbau entwickelter Rechenverfahren," *Med. orthop. Tech.*, vol. 6, pp. 130–138, 1975.

[57]   H. Olofsson, "Three dimensional FEM calculation of elastic stress field in human femur," University of Uppsala, 1976.

[58]   T. D. Brown and A. B. Ferguson, "The development of a computational stress analysis of the femoral head. Mapping tensile, compressive, and shear stress for the varus and valgus positions.," *J. Bone Joint Surg. Am.*, vol. 60, no. 5, pp. 619–29, Jul. 1978.

[59]   W. C. Hayes and B. Snyder, "Correlations between stress and morphology in trabecular bone of the patella," in *Proceedings of the 25th Annual Meeting of the Orthopaedic Research Society*, 1979, p. 88.

[60]   W. C. Hayes, B. Snyder, B. M. Levine, and S. Ramaswamy, "Stress-morphology relationships in trabecular bone of the patella," in *Finite Elements in Biomechanics*, New York: John Wiley, 1982, pp. 223–268.

[61]   T. P. Andriacchi, J. O. Galante, T. B. Belytschko, and S. Hampton, "A stress analysis of the femoral stem in total hip prostheses.," *J. Bone Joint Surg. Am.*, vol. 58, no. 5, pp. 618–24, Jul. 1976.

[62]   B. M. Kwak, O. K. Lim, Y. Y. Kim, and K. Rim, "An investigation of the effect of cement thickness on an implant by finite element stress analysis," *Int. Orthop.*, vol. 2, no. 4, pp. 315–319, 1979.

[63]   G. C. Sih, P. Matic, and A. T. Berman, "Failure prediction of the total hip prosthesis system," *J. Biomech.*, vol. 14, no. 12, pp. 833–841, Jan. 1981.

[64]   H. Roehrle, R. Scholten, W. Sollbach, G. Ritter, and A. Gruenert, "Der Kraftfluss bei Huftendoprothesen," *Arch. orthop. Unfailchir*, vol. 89, pp. 49–60, 1977.

[65]   S. Valliappan, S. Kjellberg, and N. L. Svensson, "Finite element analysis of total hip prosthesis," in *International Conference Proceedings on Finite Elements in Biomechanics*, 1980, pp. 528-548.

[66]   J. L. Lewis, G. M. Kramer, R. L. Wixson, and M. J. Askew, "Calcar loading by titanium total hip stems," in *Proceedings 27th Annual Meeting Orthopaedic Research Society*, 1981, p. 75.

[67]   S. C. Anand, K. R. St. John, D. D. Moyle, and D. F. Williams, "Finite element analysis of a medullary shaft implant," in *Proceedings 29th Annual Conference on Engineering in Medicine and Biology*, 1976, p. 245.

[68]   P. Ducheyne, E. Aernoudt, P. De Meester, M. Martens, J. C. Mulier, and D. Van Leeuwen, "Factors governing the mechanical behavior of the implant-porous coating-trabecular bone interface," *J. Biomech.*, vol. 11, no. 6–7, pp. 297-307, Jan. 1978.

[69]   R. Vasu, D. R. Carter, and W. H. Harris, "Stress distributions in the acetabular region--I. Before and after total joint replacement.," *J. Biomech.*, vol. 15, no. 3, pp. 155–64, 1982.

[70]   D. R. Carter, R. Vasu, and W. H. Harris, "Stress distributions in the acetabular region--II. Effects of cement thickness and metal backing of the total hip acetabular component.," *J. Biomech.*, vol. 15, no. 3, pp. 165–70, 1982.

[71]   H. Oonishi, "Three-dimensional finite element analysis of the pelvis and ceramic acetabulum.," in *Proceedings 27th Annual Meeting Orthopaedic Research Society*, 1981, p. 72.

[72]   V. K. Goel, S. Valliappan, and N. L. Svensson, "Stresses in the pelvis fitted with Charnley and McKee-Farrar prostheses.," 1981.

[73]   P. Prendergast, "Finite element models in tissue mechanics and orthopaedic implant design," *Clin. Biomech.*, vol. 12, no. 6, pp. 343–366, Sep. 1997.

[74]   H. A. Hogan, "Micromechanics modeling of Haversian cortical bone properties.," *J. Biomech.*, vol. 25, no. 5, pp. 549–56, May 1992.

[75]   G. S. Beaupre and W. C. Hayes, "Finite element analysis of a three-dimensional open-celled model for trabecular bone.," *J. Biomech. Eng.*, vol. 107, no. 3, pp. 249–56, Aug. 1985.

[76]   T. D. Brown and G. L. Hild, "Pre-collapse stress redistributions in femoral head osteonecrosis--a three-dimensional finite element analysis.," *J. Biomech. Eng.*, vol. 105, no. 2, pp. 171–6, May 1983.

[77]   J. C. Lotz, E. J. Cheal, and W. C. Hayes, "Fracture prediction for the proximal femur using finite element models: Part II--Nonlinear analysis.," *J. Biomech. Eng.*, vol. 113, no. 4, pp. 361–5, Nov. 1991.

[78]   A. Rohlmann, U. Mössner, G. Bergmann, and R. Kölbel, "Finite-element-analysis and experimental investigation in a femur with hip endoprosthesis.," *J. Biomech.*, vol. 16, no. 9, pp. 727–42, 1983.

[79]   M. J. Fagan and A. J. Lee, "Role of the collar on the femoral stem of cemented total hip replacements.," *J. Biomed. Eng.*, vol. 8, no. 4, pp. 295–304, Oct. 1986.

[80]   P. J. Prendergast and D. Taylor, "Stress analysis of the proximo-medial femur after total hip replacement.," *J. Biomed. Eng.*, vol. 12, no. 5, pp. 379–82, Sep. 1990.

[81]   E. G. Little, A. G. Kneafsey, P. Lynch, and M. Kennedy, "The design of a model for a three dimensional stress analysis of the cement layer beneath the medial plateau of a knee prosthesis.," *J. Biomech.*, vol. 18, no. 2, pp. 157–60, 1985.

[82]   R. Huiskes and W. Vroemen, "A standardised finite element model for routine comparative evaluations of femoral hip prostheses," *Acta Orthop. Belg.*, vol. 319, pp. 64–76, 1986.

[83]   R. Huiskes, H. Weinans, and M. Dalstra, "Adaptive bone remodeling and biomechanical design considerations : for noncemented total hip arthroplasty Huiskes ct aJ ADAPTIVE BONE REMODELING Adaptive Bone Remodeling and Biomechanical Design Considerations for Noncemented Thtal ffip Arthroplasty," *Orthopaedics*, vol. 12, pp. 1255–1267, 1989.

[84]   M. Viceconti, B. P. McNamara, A. Toni, and A. Giunti, "FEM analysis of the static stresses induced in a THR femoral components during a standardized fatigue test," *Comput. Methods Biomech. Biomed. Engin.*, pp. 57–66, 1996.

[85]   S. Poelert, E. Valstar, H. Weinans, and A. A. Zadpoor, "Patient-specific finite element modeling of bones," *Proc. Inst. Mech. Eng. Part H J. Eng. Med.*, vol. 227, no. 4, pp. 464–478, Apr. 2013.

[86]   J. P. Little, F. Taddei, M. Viceconti, D. W. Murray, and H. S. Gill, "Changes in femur stress after hip resurfacing arthroplasty: Response to physiological loads," *Clin. Biomech.*, vol. 22, no. 4, pp. 440–448, May 2007.

[87]   M. R. Abdul-Kadir, U. Hansen, R. Klabunde, D. Lucas, and A. Amis, "Finite element modelling of primary hip stem stability: The effect of interference fit," *J. Biomech.*, vol. 41, no. 3, pp. 587–594, Jan. 2008.

[88]   D. D. Cody, G. J. Gross, F. J. Hou, H. J. Spencer, S. A. Goldstein, and D. P. Fyhrie, "Femoral strength is better predicted by finite element models than QCT and DXA.," *J. Biomech.*, vol. 32, no. 10, pp. 1013-20, Oct. 1999.

[89]   E. Tanck *et al.*, "Pathological fracture prediction in patients with metastatic lesions can be improved with quantitative computed tomography based computer models," *Bone*, vol. 45, no. 4, pp. 777–783, Oct. 2009.

[90]   J. Graça, "Ferramenta numérica para discretização do fémur a partir de radiografia", Universidade do Porto, 2017.

[91]   S. M. Kazemi, M. Qoreishy, A. Keipourfard, M. M. Sajjadi, and S. Shokraneh, "Effects of Hip Geometry on Fracture Patterns of Proximal Femur.," *Arch. bone Jt. Surg.*, vol. 4, no. 3, pp. 248–52, Jun. 2016.

[92]   D. L. Polishchuk, D. A. Patrick, B. V. Gvozdyev, J. H. Lee, J. A. Geller, and W. Macaulay, "Predicting Femoral Head Diameter and Lesser Trochanter to Center of Femoral Head Distance: A Novel Method of Templating Hip Hemiarthroplasty," *J. Arthroplasty*, vol. 28, no. 9, pp. 1603–1607, Oct. 2013.

[93]   Y. Lai, W.-C. Chen, and C.-H. Huang, "The Effect of Graft Strength on Knee Laxity and Graft In-Situ Forces after Posterior Cruciate Ligament Reconstruction," *PLoS One*, vol. 10, no. 5, 2015.

[94]   J. Belinha, R. M. Natal Jorge, and L. M. J. S. Dinis, "Bone tissue remodelling analysis considering a radial point interpolator meshless method," *Eng. Anal. Bound. Elem.*, vol. 36, no. 11, pp. 1660–1670, Nov. 2012.

[95]   G. S. Beaupré, T. E. Orr, and D. R. Carter, "An approach for time-dependent bone modeling and remodeling-application: A preliminary remodeling simulation," *J. Orthop. Res.*, vol. 8, no. 5, pp. 662–670, Sep. 1990.

[96]   E. F. Rybicki, F. A. Simonen, and E. B. Weis, "On the mathematical analysis of stress in the human femur," *J. Biomech.*, vol. 5, no. 2, pp. 203-215, Mar. 1972.

[97]   A. Törzeren, *Human Body Dynamics Classical Mechanics and Human Movement*, Springer, 1999